SIAM J. SCI. COMPUT.
Vol. 37, No. 6, pp. B855–B883

OPTIMAL SHAPE DESIGN BY PARTIAL SPECTRAL DATA*

HABIB AMMARI†, YAT TIN CHOW‡, KEJI LIU§, AND JUN ZOU¶

Abstract. In this paper, we are concerned with a shape design problem, in which our target is to design, up to rigid transformations and scaling, the shape of an object given either its polarization tensor at multiple contrasts or the partial eigenvalues of its Neumann–Poincaré operator, which are known as the Fredholm eigenvalues. We begin by proposing to recover the eigenvalues of the Neumann–Poincaré operator from the polarization tensor by means of the holomorphic functional calculus. Then we develop a regularized Gauss–Newton optimization method for the shape reconstruction process. We present numerical results to demonstrate the effectiveness of the proposed methods and to illustrate important properties of the Fredholm eigenvalues and their associated eigenfunctions. Our results are expected to have important applications in the design of plasmon resonances in nanoparticles as well as in the multifrequency or pulsed imaging of small anomalies.

Key words. optimal shape design, plasmonics, polarization tensor, Fredholm eigenvalues, Neumann–Poincaré operator, pulsed electrical capacitance tomography

AMS subject classifications. 49J20, 47A75, 35R30, 35B30

DOI. 10.1137/130942498

1. Introduction.

Fredholm eigenvalues are the eigenvalues of the integral Neumann–Poincaré operator, which arises naturally in solving Neumann transmission problems for the Laplacian. They depend on the shape of the domain but they are invariant under rigid transformations and scaling. They have been the subject of intensive investigations; see, for instance, [1, 33, 34, 36]. Spectral analysis of Neumann–Poincaré type operators has played a key role in the mathematical justification of cloaking due to anomalous localized resonance [5] and in the analysis of gradient blow-up phenomena in the presence of nearly touching inclusions [6, 15, 16]. We also refer to [26], where new and interesting facts on spectral analysis related to the Neumann–Poincaré integral operator have been obtained, and to the works on plasmon resonances [22, 29, 30]. Plasmon resonant nanoparticles such as gold nanoparticles offer, in addition to their biocompatibility, enhanced scattering and absorption, making them suitable not only for use as a contrast agent but also in therapeutic applications [22]. Recently, it has been shown that plasmon resonances in nanoparticles can be treated as an eigenvalue problem for the Neumann–Poincaré operator, which leads to direct calculation of resonance values of permittivity and

*Submitted to the journal's Computational Methods in Science and Engineering section October 23, 2013; accepted for publication (in revised form) September 15, 2015; published electronically November 19, 2015.

http://www.siam.org/journals/sisc/37-6/94249.html

†Department of Mathematics and Applications, Ecole Normale Supérieure, 45 Rue dUlm, 75005 Paris, France (habib.ammari@ens.fr). The work of this author was supported by ERC Advanced Grant Project MULTIMOD–267184.

‡Department of Mathematics, University of California, Los Angeles, 520 Portola Plaza, Math Sciences Building 6363, Los Angeles, CA 90095 (ytchow@math.ucla.edu).

§Shanghai Key Laboratory of Financial Information Technology, School of Finance, Shanghai University of Finance and Economics, 777 Guoding Road, Shanghai 200433, China (liu.keji@mail.shufe.edu.cn). The work of this author was substantially supported by the Science and Technology Commission of Shanghai Municipality under grants 14511107200 and 15511107302.

¶Department of Mathematics, The Chinese University of Hong Kong, Shatin, NT, Hong Kong (zou@math.cuhk.edu.hk). The work of this author was substantially supported by Hong Kong RGC grants (projects 405513 and 404611).

resonance frequency [7, 18, 30]. In biomedical applications, it is challenging to design nanoparticles that resonate at specified frequencies. It is the purpose of the paper to propose an efficient approach for solving the optimal design problem (up to rigid transformations and scaling) from partial Fredholm eigenvalues.

Shape identification from Fredholm eigenvalues also has important applications in imaging. In electrosensing, the polarization tensor of a target at multiple frequencies (or equivalently at multiple contrasts) can be reconstructed from electrical capacitance measurements [2, 3, 4, 27, 35]. The polarization tensor arises naturally when we describe the perturbation of the electrical potential due to the presence of the target whose admittivity is different from that of the background. In fact, the polarization tensor of an inclusion can be expressed in terms of the Neumann–Poincaré operator and the admittivity contrast.

In this paper, we first show that the Fredholm eigenvalues can be reconstructed from the polarization tensor at multiple contrasts. By doing so, we connect design problems for plasmon resonances in nanoparticles to the imaging of small anomalies. Moreover, we show how to obtain in practice the polarization tensor at multiple contrasts from electrical capacitance tomography measurements. By probing the domain with an electric pulse, the polarization tensor of the anomaly at multiple frequencies and therefore at multiple contrasts can be recovered [20, 28]; see Appendix A. We optimize the pulse shape in order to reconstruct in the most stable way the first few Fredholm eigenvalues.

Then we consider the shape reconstruction problem (up to rigid transformations and scaling), in which we wish to reconstruct a shape from only the prior knowledge of the first several Fredholm eigenvalues of the Neumann–Poincaré operator. We start by giving both analytical and numerical evidence that the first Fredohlm eigenvalues contain only low-frequency information about the shape of the domain while higher ones contain higher-frequency information. We estimate the oscillation behavior of the associated eigenfunctions. We also emphasize the exponential decay of the Fredholm eigenvalues in the two-dimensional case. This clearly makes the design problem exponentially ill-posed. Therefore, we should restrict ourselves to low-frequency shape reconstructions from the first few Fredholm eigenvalues.

We also derive Hadamard's formula for the Fredholm eigenvalues. Based on Osborn's theorem [31], we compute the shape derivative of Fredholm eigenvalues using the shape derivative of the Neumann–Poincaré operator. Then we propose a minimization algorithm to reconstruct a domain given its first Fredholm eigenvalues. In view of the invariance of the Fredholm eigenvalues under rigid transformations and scaling, we incorporate some effective penalty and regularization terms in the cost functional to ensure the local existence and uniqueness of its minimizers. We will further present several numerical illustrations of our main findings.

Our results on Fredholm eigenvalues and on the polarization tensor are expected to have important applications not only in shape design problems but also in shape classification and recognition problems. Various other geometric quantities associated with the shape of a domain, such as eigenvalues, capacities, harmonic moments, and generalized polarization tensors, are used to distinguish between objects and classify them [3, 8, 9, 12, 14, 17, 21, 23]. The concept of polarization tensor at multiple contrasts seems to be the most natural one for shape classification and recognition using capacitance electrical impedance tomography.

The paper is organized as follows. In section 2, we introduce the Neumann–Poincaré operator and the concept of polarization tensor associated with a given domain and a given contrast. In section 3, two methods are provided for reconstructing Fredholm eigenvalues of a domain from its polarization tensor at all contrasts then

tested numerically. Section 4 is devoted to the derivation of a Hadamard's perturbation formula for Fredholm eigenvalues. By combining the results in [12] on the shape derivative of the Neumann–Poincaré operator together with Osborn's theorem [31], we compute the shape derivative of Fredholm eigenvalues. In section 5, we present and numerically test our minimization procedure for finding low-frequency features of a domain from its first few Fredholm eigenvalues. In Appendix A, we show the method to obtain the polarization tensors at multiple contrasts from electrical capacitance tomography measurements. In Appendix B, we consider the case of multiply connected objects. In that case, it is remarkable to easily find the number of connected components from the multiplicity of the Fredholm eigenvalues.

2. Neumann–Poincaré operator and polarization tensor. In this section, we first introduce the Neumann–Poincaré operator of an open connected domain D with $\mathcal{C}^2$ boundary in $\mathbb{R}^d$ $(d = 2, 3)$. Given such a domain D, we consider the Neumann problem

$$\Delta u = 0 \quad \text{in} \quad D\,; \qquad \frac{\partial u}{\partial \nu} = g \quad \text{on} \quad \partial D, \qquad \int_{\partial D} u \, d\sigma = 0, \tag{2.1}$$

where $g \in L^2_0(\partial D)$ with $L^2_0(\partial D)$ is the set of functions in $L^2(\partial D)$ with zero mean-value. In (2.1), $\partial/\partial\nu$ denotes the normal derivative. We note that the Neumann problem (2.1) can be rewritten as a boundary integral equation with the help of the single-layer potential. Given a density function $\phi \in L^2(\partial D)$, the single-layer potential, $\mathcal{S}_{\partial D}[\phi]$, can be defined as

$$\mathcal{S}_{\partial D}[\phi](x) := \int_{\partial D} \Gamma(x - y)\phi(y) d\sigma(y) \tag{2.2}$$

for $x \in \mathbb{R}^d$, where Γ is the fundamental solution of the Laplacian in $\mathbb{R}^d$:

$$\Gamma(x - y) = \begin{cases} -\frac{1}{2\pi} \log |x - y| & \text{if } \ d = 2\,, \\ \frac{1}{(2-d)\omega_d} |x - y|^{2-d} & \text{if } \ d > 2\,, \end{cases} \tag{2.3}$$

where ω_d denotes the surface area of the unit sphere in $\mathbb{R}^d$. It is well-known that the single-layer potential satisfies the following jump condition on ∂D:

$$\frac{\partial}{\partial \nu} \left(\mathcal{S}_{\partial D}[\phi]\right)^{\pm} = \left(\pm\frac{1}{2} I + \mathcal{K}^*_{\partial D}\right)[\phi]\,, \tag{2.4}$$

where the superscripts $\pm$ indicate the limits from outside and inside D, respectively, and $\mathcal{K}^*_{\partial D} : L^2(\partial D) \to L^2(\partial D)$ is the Neumann–Poincaré operator defined by

$$\mathcal{K}^*_{\partial D}[\phi](x) := \frac{1}{\omega_d} \int_{\partial D} \frac{\langle x - y, \nu_x \rangle}{|x - y|^d} \phi(y) d\sigma(y) \tag{2.5}$$

with ν_x being the outward normal at $x \in \partial D$. We note that $\mathcal{K}^*_{\partial D}$ maps $L^2_0(\partial D)$ onto itself.

With these notions, the Neumann problem (2.1) can then be formulated as

$$g = \frac{\partial}{\partial \nu} \left(\mathcal{S}_{\partial D}[\phi]\right)^{-} = \left(-\frac{1}{2} I + \mathcal{K}^*_{\partial D}\right)[\phi]\,. \tag{2.6}$$

Therefore, the solution to the Neumann problem (2.1) can be reformulated as a solution to the boundary integral equation with the Neumann–Poincaré operator $\mathcal{K}^*_{\partial D}$.

The operator $\mathcal{K}^*_{\partial D}$ arises not only in solving the Neumann problem for the Laplacian but also for representing the solution to the transmission problem as described below.

Consider an open connected domain D with $\mathcal{C}^2$ boundary in $\mathbb{R}^d$. Given a harmonic function u_0 in $\mathbb{R}^d$, we consider the following transmission problem in $\mathbb{R}^d$:

$$\begin{cases} \nabla \cdot (\varepsilon_D \nabla u) = 0 & \text{in } \mathbb{R}^d, \\ u - u_0 = O(|x|^{1-d}) & \text{as } |x| \to \infty, \end{cases} \tag{2.7}$$

where $\varepsilon_D = \varepsilon_c \chi(D) + \varepsilon_m \chi(\mathbb{R}^d \backslash \overline{D})$ with $\varepsilon_c, \varepsilon_m$ being two positive constants, and $\chi(\Omega)$ is the characteristic function of the domain $\Omega = D$ or $\mathbb{R}^d \backslash \overline{D}$. With the help of the single-layer potential, we can rewrite the perturbation $u - u_0$, which is due to the inclusion D, as

$$u - u_0 = \mathcal{S}_{\partial D}[\phi]\,, \tag{2.8}$$

where $\phi \in L^2(\partial D)$ is an unknown density, and $\mathcal{S}_{\partial D}[\phi]$ is the refraction part of the potential in the presence of the inclusion. The transmission problem (2.7) can be rewritten as

$$\begin{cases} \Delta u = 0 & \text{in } D \bigcup (\mathbb{R}^d \backslash \overline{D})\,, \\ u^+ = u^- & \text{on } \partial D\,, \\ \varepsilon_c \frac{\partial u^+}{\partial \nu} = \varepsilon_m \frac{\partial u^-}{\partial \nu} & \text{on } \partial D\,, \\ u - u_0 = O(|x|^{1-d}) & \text{as } |x| \to \infty\,. \end{cases} \tag{2.9}$$

With the help of the jump condition (2.4), solving the above system (2.9) can be regarded as solving the density function $\phi \in L^2(\partial D)$ of the following integral equation:

$$\frac{\partial u_0}{\partial \nu} = \left(\frac{\varepsilon_c + \varepsilon_m}{2(\varepsilon_c - \varepsilon_m)} I - \mathcal{K}^*_{\partial D} \right) [\phi]\,. \tag{2.10}$$

With the harmonic property of u_0, we can write

$$u_0(x) = \sum_{\alpha \in \mathbb{N}^d} \frac{1}{\alpha!} \partial^\alpha u_0(0) x^\alpha \tag{2.11}$$

with $\alpha = (\alpha_1, \ldots, \alpha_d) \in \mathbb{N}^d$, $\partial_\alpha = \partial_1^{\alpha_1} \ldots \partial_d^{\alpha_d}$, and $\alpha! = \alpha_1! \ldots \alpha_d!$.

Consider ϕ^α as the solution of the Neumann–Poincaré operator:

$$\frac{\partial x^\alpha}{\partial \nu} = \left(\frac{\varepsilon_c + \varepsilon_m}{2(\varepsilon_c - \varepsilon_m)} I - \mathcal{K}^*_{\partial D} \right) [\phi^\alpha]\,. \tag{2.12}$$

The invertibilities of the operator $(\frac{\varepsilon_c + \varepsilon_m}{2(\varepsilon_c - \varepsilon_m)} I - \mathcal{K}^*_{\partial D})$ from $L^2(\partial D)$ onto $L^2(\partial D)$ and from $L^2_0(\partial D)$ onto $L^2_0(\partial D)$ are proved, for example, in [10, 25], provided that $|\frac{\varepsilon_c + \varepsilon_m}{2(\varepsilon_c - \varepsilon_m)}| > 1/2$. We can substitute (2.11) and (2.12) back into (2.8) to get

$$u - u_0 = \sum_{|\alpha| \geq 1} \frac{1}{\alpha!} \partial^\alpha u_0(0) \mathcal{S}_{\partial D}[\phi^\alpha] = \sum_{|\alpha| \geq 1} \frac{1}{\alpha!} \partial^\alpha u_0(0) \int_{\partial D} \Gamma(x - y) \phi^\alpha(y) d\sigma(y)\,. \tag{2.13}$$

Using the Taylor expansion,

$$\Gamma(x - y) = \Gamma(x) - y \cdot \nabla \Gamma(x) + O\left(\frac{1}{|x|^d} \right)\,, \tag{2.14}$$

which holds for all x such that $|x| \to \infty$ while y is bounded [10], we get the result by substituting (2.14) into (2.13) that

$$(u-u_0)(x) = \nabla u_0(0) \cdot M(\lambda, D)\nabla\Gamma(x) + O\left(\frac{1}{|x|^d}\right) \quad \text{as} \quad |x| \to \infty, \tag{2.15}$$

where $M = (M_{ij})_{i,j=1}^d$ is the polarization tensor associated with the domain D and the contrast λ defined by

$$M_{ij}(\lambda, D) := \int_{\partial D} y_i (\lambda I - \mathcal{K}_{\partial D}^*)^{-1} [\nu_j](y) d\sigma(y) \tag{2.16}$$

with $\lambda := \frac{\varepsilon_c + \varepsilon_m}{2(\varepsilon_c - \varepsilon_m)}$ and ν_j being the jth component of ν. Here we have used in (2.15) the fact that $\int_{\partial D} \nu \, d\sigma = 0$.

Typically the constants ε_c and ε_m are positive in order to make the system (2.9) physical. This corresponds to the situation with $|\lambda| > \frac{1}{2}$.

However, recent advances in nanotechnology make it possible to produce noble metal nanoparticles with negative permittivities at optical frequencies [22, 32]. Therefore, we can have the possibility for some frequencies that $\lambda := \frac{\varepsilon_c + \varepsilon_m}{2(\varepsilon_c - \varepsilon_m)}$ actually lies in the spectrum of $\mathcal{K}_{\partial D}^*$.

If this happens, the integral equation

$$0 = (\lambda I - \mathcal{K}_{\partial D}^*)[\phi] \quad \text{on} \quad \partial D \tag{2.17}$$

has nontrivial solutions $\phi \in L^2(\partial D)$ and the nanoparticle resonates at those frequencies.

Therefore, we have to investigate the mapping properties of the Neumann–Poincaré operator. Assume that ∂D is of class $\mathcal{C}^{1,\alpha}$. It is known that the operator $\mathcal{K}_{\partial D}^* : L^2(\partial D) \to L^2(\partial D)$ is compact [25], and its spectrum is discrete and accumulates at zero. All the eigenvalues are real and bounded by $1/2$. Moreover, $1/2$ is always an eigenvalue and its associated eigenspace is of dimension one, which is nothing else but the kernel of the single-layer potential $\mathcal{S}_{\partial D}$. In two dimensions, it can be proved that if $\lambda_i \neq 1/2$ is an eigenvalue of $\mathcal{K}_{\partial D}^*$, then $-\lambda_i$ is an eigenvalue as well. This property is known as the twin spectrum property; see [29]. The Fredholm eigenvalues are the eigenvalues of $\mathcal{K}_{\partial D}^*$. It is easy to see, from the properties of $\mathcal{K}_{\partial D}^*$, that they are invariant with respect to rigid motions and scaling. They can be explicitly computed for ellipses and spheres. If a and b denote the semi-axis lengths of an ellipse, then it can be shown that $\pm(\frac{a-b}{a+b})^i$ are its Fredholm eigenvalues [26]. For the sphere, they are given by $1/(2(2i+1))$; see [24]. It is worth noticing that the convergence to zero of Fredholm eigenvalues is exponential for ellipses while it is algebraic for spheres.

Equation (2.17) corresponds to the case when plasmonic resonance occurs in D; see [18]. The optimal shape design for Fredholm eigenvalues is of great interest in plasmonics [22, 29, 32]. Given negative values of ε_c, we show in this paper how to design a shape with prescribed plasmonic resonances.

3. Reconstruction of Fredholm eigenvalues from the polarization tensor.

3.1. Reconstruction method via holomorphic functional calculus. In this subsection we propose for two dimensions to recover the Fredholm eigenvalues

from the polarization tensor

$$M(\lambda, D) := \int_{\partial D} y(\lambda I - \mathcal{K}_{\partial D}^*)^{-1}[\nu](y)d\sigma(y) \tag{3.1}$$

for λ along a simple closed curve γ by means of the holomorphic functional calculus. From this expression, one observes that $M(\lambda, D)$ actually encodes vast information of the resolvent of the operator $\mathcal{K}_{\partial D}^*$ at λ,

$$R_\lambda(\mathcal{K}_{\partial D}^*) := (\lambda I - \mathcal{K}_{\partial D}^*)^{-1}. \tag{3.2}$$

Motivated by this observation, we propose to recover eigenvalues $\{\lambda_i\}_{i\geq 1}$ ($\lambda_i \neq 1/2$) of $\mathcal{K}_{\partial D}^*$ from $M(\lambda, D)$ via the holomorphic functional calculus of $\mathcal{K}_{\partial D}^*$. Let $\mathcal{H}$ be the space $L_0^2(\partial D)$ equipped with the inner product $-\langle \cdot, \mathcal{S}_{\partial D}(\cdot)\rangle_{L^2(\partial D)}$. Since $\mathcal{S}_{\partial D}$ is injective on $L_0^2(\partial D)$, $L_0^2(\partial D)$ is complete for this inner product. If ∂D is of class $\mathcal{C}^{1,\alpha}$, there exists a complete orthonormal set $\{\phi_i^\pm\}_{i\geq 1}$ in $\mathcal{H}$ such that $\mathcal{K}_{\partial D}^*\phi_i^\pm = \pm\lambda_i\phi_i^\pm$ for all $i \geq 1$ and the eigenvalues $1/2 > \lambda_1 \geq \cdots \geq \lambda_i \to 0$ as $i \to \infty$, by using the self-adjointness and the compactness of the operator $\mathcal{K}_{\partial D}^*$ over $\mathcal{H}$ and the Hilbert–Schmidt theorem; see [26]. For notation's sake, we will often write $\lambda_i^\pm := \pm\lambda_i$ in our subsequent discussions. Then we can decompose the operator $\mathcal{K}_{\partial D}^*$ as

$$\begin{aligned}\mathcal{K}_{\partial D}^* &= \sum_{i=1}^{\infty} \left\{ \lambda_i^+ \langle \phi_i^+, \cdot\rangle_{\mathcal{H}}\ \phi_i^+ + \lambda_i^- \langle \phi_i^-, \cdot\rangle_{\mathcal{H}}\ \phi_i^- \right\} \\ &= \sum_{i=1}^{\infty} \lambda_i \left\{ \langle \phi_i^+, \cdot\rangle_{\mathcal{H}}\ \phi_i^+ - \langle \phi_i^-, \cdot\rangle_{\mathcal{H}}\ \phi_i^- \right\}.\end{aligned} \tag{3.3}$$

Note that as $\mathcal{K}_{\partial D}^*$ is a pseudodifferential operator of order -1, the eigenfunctions $\phi_i^\pm$ oscillate as $1/\lambda_i$, and there exists a positive constant C such that

$$\frac{||\frac{\partial \phi_i^\pm}{\partial T}||_{L^2(\partial D)}}{||\phi_i^\pm||_{L^2(\partial D)}} \lesssim \frac{C}{\lambda_i},$$

where $\partial/\partial T$ denotes the tangential derivative.

Now, given the Neumann–Poincaré operator $\mathcal{K}_{\partial D}^*$ corresponding to a shape D (D being an open domain with $\mathcal{C}^{1,\alpha}$ boundary), we define, for any holomorphic function f on an open domain $U \subset \mathbb{C}$ containing the spectrum of $\mathcal{K}_{\partial D}^*$, the following notion:

$$f(\mathcal{K}_{\partial D}^*) := \sum_{i=1}^{\infty} \left[f(\lambda_i^+)\langle \phi_i^+, \cdot\rangle_{\mathcal{H}}\, \phi_i^+ + f(\lambda_i^-)\langle \phi_i^-, \cdot\rangle_{\mathcal{H}}\, \phi_i^- \right]. \tag{3.4}$$

Clearly, if f is a polynomial in $z \in \mathbb{C}$, say, $f(z) := \sum_{i=0}^N a_i z^i$ for some $N \in \mathbb{N}$, the definition (3.4) coincides with the conventional one, i.e., $f(\mathcal{K}_{\partial D}^*) = \sum_{i=0}^N a_i \left(\mathcal{K}_{\partial D}^*\right)^i$, where $\left(\mathcal{K}_{\partial D}^*\right)^i$ means the composition of the operator i times. For our subsequent description, we may write for any $\phi \in L^2(\partial D)$ that

$$\langle \phi, y\rangle_{L^2(\partial D)} := \int_{\partial D} y\phi(y)d\sigma(y).$$

Then we have the following representation result.

LEMMA 3.1. *Given a shape D and the corresponding Neumann–Poincaré operator $\mathcal{K}_{\partial D}^*$, the following identity holds for the polarization tensor $M(\lambda, D)$ in* (3.1) *and any*

holomorphic function f on an open domain $U \subset \mathbb{C}$ containing the spectrum $\sigma(\mathcal{K}^*_{\partial D})$ of $\mathcal{K}^*_{\partial D}$:

$$\frac{1}{2\pi i}\int_\gamma f(\lambda)M(\lambda,D)d\lambda = \int_{\partial D} y f(\mathcal{K}^*_{\partial D})[\nu](y)d\sigma(y) = \sum_{i=1}^{\infty}\left[c_i^+ f(\lambda_i^+) + c_i^- f(\lambda_i^-)\right], \tag{3.5}$$

where γ is an arbitrary simple closed curve in U enclosing $\sigma(\mathcal{K}^*_{\partial D})$, and c_i^+ and c_i^- are defined by

$$c_i^+ := \langle \nu, \phi_i^+\rangle_{\mathcal{H}}\langle \phi_i^+, y\rangle_{L^2(\partial D)}, \quad c_i^- := \langle \nu, \phi_i^-\rangle_{\mathcal{H}}\langle \phi_i^-, y\rangle_{L^2(\partial D)}. \tag{3.6}$$

Proof. By the holomorphic functional calculus, we know for any holomorphic function f on an open domain $U \subset \mathbb{C}$ containing $\sigma(\mathcal{K}^*_{\partial D})$ and any simple closed curve γ in U enclosing $\sigma(\mathcal{K}^*_{\partial D})$ that

$$\frac{1}{2\pi i}\int_\gamma f(\lambda)R_\lambda(\mathcal{K}^*_{\partial D})d\lambda = f(\mathcal{K}^*_{\partial D}) = \sum_{i=1}^{\infty}\left[f(\lambda_i^+)\langle \phi_i^+, \cdot\rangle_{\mathcal{H}}\,\phi_i^+ + f(\lambda_i^-)\langle \phi_i^-, \cdot\rangle_{\mathcal{H}}\,\phi_i^-\right]. \tag{3.7}$$

Combining this with (3.1), we readily derive that

$$\frac{1}{2\pi i}\int_\gamma f(\lambda)M(\lambda,D)d\lambda = \int_{\partial D} y f(\mathcal{K}^*_{\partial D})[\nu](y)d\sigma(y). \tag{3.8}$$

Now the desired representation comes from the above two identities. ∎

We note that even if ∂D is only Lipschitz, a similar result can be obtained for the (noncompact) operator $\mathcal{K}^*_{\partial D}$ from the spectral decomposition $\mathcal{K}^*_{\partial D} = \int \lambda dE_\lambda$, where E_λ is the projection-valued measure. However, we will not pursue this direction for the sake of simplicity. We refer the reader to [19].

Based on the relation (3.5), we can make use of different choices of holomorphic functions f to reconstruct the eigenvalues λ_i of $\mathcal{K}^*_{\partial D}$ from its polarization tensor. One of the methods is based on the following observation. For any $n \in \mathbb{N}$ we define

$$h_1^{(n)} := \frac{1}{2\pi i}\int_\gamma \lambda^{2n} M(\lambda,D)d\lambda, \tag{3.9}$$

$$h_j^{(n)} := \frac{1}{2\pi i}\int_\gamma \lambda^{2n} M(\lambda,D)d\lambda - \sum_{i=1}^{j-1}\left(c_i^+ + c_i^-\right)\lambda_i^{2n} \quad \text{for } j > 1; \tag{3.10}$$

then we come to the following corollary.

Corollary 3.2. *Assume that all the eigenvalues of $\mathcal{K}^*_{\partial D}$ are simple. Then for any $j \in \mathbb{N}$ such that $c_j^+ + c_j^- \neq 0$, it holds that*

$$\lim_{n\to\infty}\frac{h_j^{(n)}}{h_j^{(n-1)}} = \lambda_j^2 \quad \text{and} \quad \lim_{n\to\infty}\frac{h_j^{(n)}}{\lambda_j^{2n}} = c_j^+ + c_j^-. \tag{3.11}$$

Proof. Taking $f = \lambda^{2n}$ for $n \in \mathbb{N}$ in (3.5), we have

$$\frac{1}{2\pi i}\int_\gamma \lambda^{2n} M(\lambda,D)d\lambda = \sum_{i=1}^{\infty}\left[c_i^+(\lambda_i)^{2n} + c_i^-(-\lambda_i)^{2n}\right] = \sum_{i=1}^{\infty}\left(c_i^+ + c_i^-\right)\lambda_i^{2n}. \tag{3.12}$$

Substituting (3.12) into (3.9)–(3.10), we get that for all $j \in \mathbb{N}$,

$$h_j^{(n)} = \sum_{i=j}^{\infty} \left(c_i^+ + c_i^-\right) \lambda_i^{2n} . \tag{3.13}$$

Noting that all the eigenvalues of $\mathcal{K}_{\partial D}^*$ are simple and $c_j^+ + c_j^- \neq 0$, we readily obtain from (3.13) that

$$\lim_{n\to\infty} \frac{h_j^{(n)}}{h_j^{(n-1)}} = \lim_{n\to\infty} \frac{\sum_{i=j}^{\infty} \left(c_i^+ + c_i^-\right) \lambda_i^{2n}}{\sum_{i=j}^{\infty} \left(c_i^+ + c_i^-\right) \lambda_i^{2(n-1)}} = \lambda_j^2 \tag{3.14}$$

and

$$\lim_{n\to\infty} \frac{h_j^{(n)}}{\lambda_j^{2n}} = \lim_{n\to\infty} \sum_{i=j}^{\infty} \left(c_i^+ + c_i^-\right) \left(\frac{\lambda_i}{\lambda_j}\right)^{2n} = c_j^+ + c_j^- . \tag{3.15}$$

This gives the conclusion of the corollary. ∎

With the help of Corollary 3.2, we can propose the following method to reconstruct the Fredholm eigenvalues from the polarization tensor at multiple contrasts.

Method 1. Given two integers $J, N \in \mathbb{N}$, for $j = 1, 2, \ldots, J$ and $n = 1, 2, \ldots, N$, compute $h_j^{(n)}$ based on (3.9)–(3.10), then compute the square root of the quotient

$$\sqrt{h_j^{(n)}/h_j^{(n-1)}}$$

for the approximation of the eigenvalue λ_j.

Next, we introduce another reconstruction method. For a $\sigma_0 > 0$, $t \in \mathbb{R}$, and a simple closed curve γ enclosing $\sigma(\mathcal{K}_{\partial D}^*)$, we define

$$\Phi_{\sigma_0,\gamma}(t) := \frac{1}{2\pi i} \int_\gamma \exp\left(-\frac{(\lambda - t)^2}{2\sigma_0^2}\right) M(\lambda, D) d\lambda . \tag{3.16}$$

Then by taking a different holomorphic function f in (3.5), we have the following useful result from Lemma 3.1.

COROLLARY 3.3. *Given a shape D and the corresponding Neumann–Poincaré operator $\mathcal{K}_{\partial D}^*$, the following equality holds:*

$$\Phi_{\sigma_0,\gamma}(t) = \sum_{i=1}^{\infty} \left[c_i^+ \exp\left(-\frac{(\lambda_i - t)^2}{2\sigma_0^2}\right) + c_i^- \exp\left(-\frac{(\lambda_i + t)^2}{2\sigma_0^2}\right)\right] . \tag{3.17}$$

Proof. For $\sigma_0 > 0$ and $t \in \mathbb{R}$, let $f(\lambda, t) := \exp(-\frac{(\lambda-t)^2}{2\sigma_0^2})$. As $f(\lambda, t)$ is holomorphic with respect to λ, we can substitute it in (3.5) to get the desired representation. ∎

Noting that the function $\exp(-\frac{(\lambda_i-t)^2}{2\sigma_0^2})$ achieves its maximum at $t = \lambda_i$ and decays exponentially away from $t = \lambda_i$, we observe from (3.17) that the local extrema of the function $\Phi_{\sigma_0,\gamma}(t)$ are approximately located at the eigenvalues λ_i of operator $\mathcal{K}_{\partial D}^*$. So we can reconstruct the eigenvalues λ_i by evaluating the local extrema of function $\Phi_{\sigma_0,\gamma}(t)$. This leads us to the following second reconstruction method.

Method 2. Given a small constant $\sigma_0 > 0$, evaluate function $\Phi_{\sigma_0,\gamma}(t)$ in (3.16) for $t \in [-1/2, 1/2]$. Then locate the local extrema of function $\Phi_{\sigma_0,\gamma}(t)$ one by one, starting from the one with the largest magnitude of $c_i^\pm$, then moving to the one with the second largest magnitude of $c_i^\pm$, and so on.

3.2. Numerical results. In this subsection, we will first present some numerical results on the approximations of the Fredholm eigenvalues and the decay properties of eigenvalues. Then we shall focus on the inverse problem to reconstruct the Fredholm eigenvalues from the observed PT at multiple contrasts.

For the approximations of the Neumann–Poincaré operator and Fredholm eigenvalues, we use a fine mesh of size $h = 1/1024$ to discretize the integral operator (2.5) by the trapezoidal quadrature rule over the curve ∂D, and we compute the eigenvalues of $\mathcal{K}^*_{\partial D}$.

For a given shape D, we plot the decay of eigenvalues and the growth of oscillation. Let λ_i be the ith eigenvalue and ϕ_i^+ be the corresponding eigenfunction. Then we define the oscillation of the eigenfunction ϕ_i^+ by

$$a_i := \frac{||\frac{\partial \phi_i^+}{\partial T}||_{L^2(\partial D)}}{||\phi_i^+||_{L^2(\partial D)}}, \quad i \geq 1. \tag{3.18}$$

In order to have an effective comparison between the scales of eigenvalues and the values of a_i in different shapes D, we normalized each of the shape D such that it has unit volume.

In Figures 1 and 2, we can see the detailed changes of λ_i, $\log \lambda_i$, and a_i against i, respectively, from which one can observe the decay of eigenvalues and the growth of oscillation of eigenfunctions, corresponding to two domains D, an ellipse of the form

$$\frac{x^2}{4} + y^2 = 1/K_1, \quad x, y \in \mathbb{R}, \tag{3.19}$$

and a heart-shaped domain of the form (with $\delta = 0.8$ and $m = 1$)

$$r = (1 + \delta \sin(m\theta))/K_2, \quad \theta \in (0, 2\pi], \tag{3.20}$$

where K_1 and K_2 are chosen such that the volumes of the corresponding shapes are 1.

Next, we carry out some numerical examples for the reconstructions of Fredholm eigenvalues from the polarization tensor at multiple contrasts. The forward data is obtained by first approximating the Neumann–Poincaré operator as done earlier in this subsection, then the polarization tensor, $M(\lambda, D) = (M_{ij}(\lambda, D))_{i,j=1}^d$, is calculated based on (3.1) using the trapezoidal rule over a fine mesh of size $h = 1/1024$ on ∂D. Values of $M(\lambda, D)$ are obtained for $\lambda \in \mathbb{C}$ on the grid points of a uniform mesh of size $1/100$ over the curve γ,

$$\gamma = \{0.23\, e^{2\pi i \theta} + 0.3 \,\big|\, 0 \leq \theta \leq 1\}, \tag{3.21}$$

and are regarded as the observed data for the reconstructions of the Fredholm eigenvalues. For the numerical comparisons, we have implemented both Methods 1 and 2 in section 3.1. We notice that, in Method 1, quadrature rules with accuracy of extremely higher orders are necessary for the approximation of the contour integration in order to accurately approximate $h_1^{(n)}$ in (3.9) for large $n \in \mathbb{N}$, which is the case for an accurate estimate of eigenvalues. Hence Method 1 may be very expensive, and we shall demonstrate only the reconstructions by Method 2 below.

By considering only those eigenvalues lying inside γ (which are all positive), we compute (3.16) in our implementations of Method 2 as follows:

$$\begin{aligned} \Phi_{\sigma_0,\gamma}(t) &:= \frac{1}{2\pi i} \int_\gamma \exp\left(-\frac{(\lambda - t)^2}{2\sigma_0^2}\right) M(\lambda, D) d\lambda \\ &= \sum_{0.07 < \lambda_i < 0.53} c_i^+ \exp\left(-\frac{(\lambda_i - t)^2}{2\sigma_0^2}\right). \end{aligned} \tag{3.22}$$

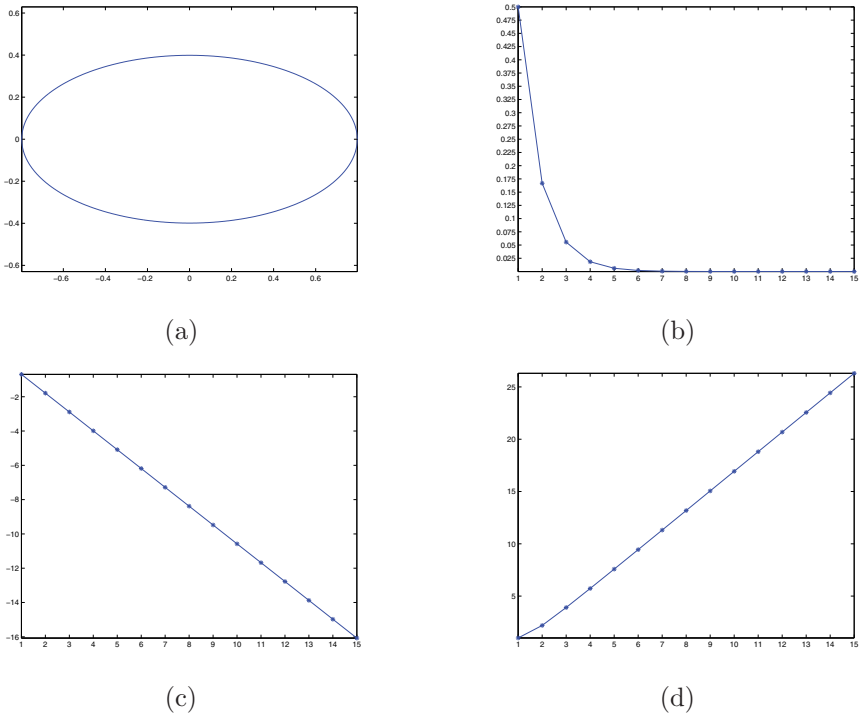

(a) (b)

(c) (d)

FIG. 1. (a) *Domain D;* (b) *λ_i against i;* (c) *$\log \lambda_i$ against i;* (d) *a_i against i.*

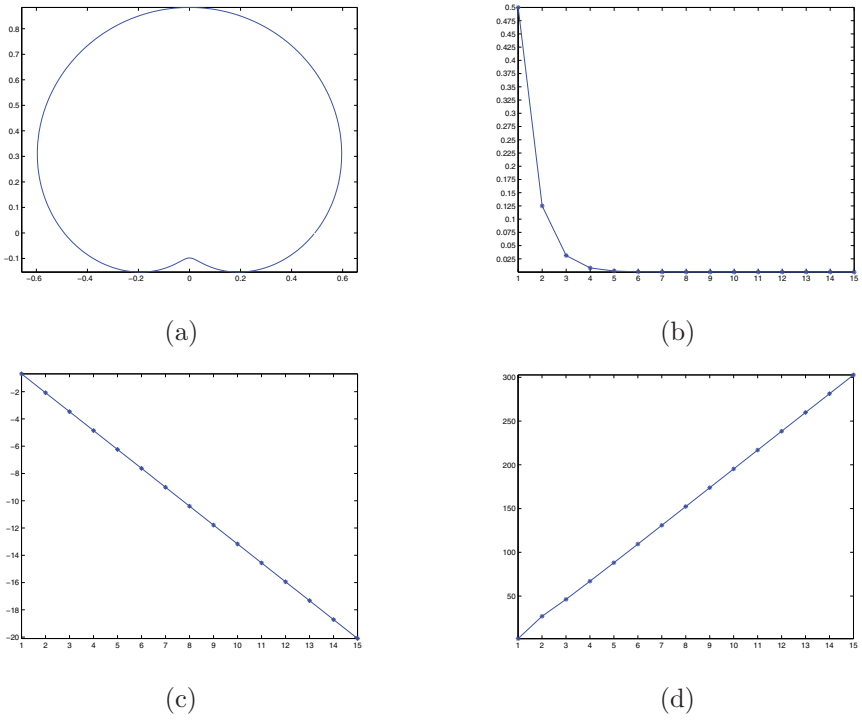

(a) (b)

(c) (d)

FIG. 2. (a) *Domain D;* (b) *λ_i against i;* (c) *$\log \lambda_i$ against i;* (d) *a_i against i.*

TABLE 1
The five reconstructed eigenvalues for the kite-shaped domain.

Eigenvalues	Exact solutions	Approximate solutions
First	0.5000	0.5000
Second	0.2707	0.2700
Third	0.1902	0.1800
Fourth	0.0891	0.0900
Fifth	0.0718	0.0700

TABLE 2
The three reconstructed eigenvalues for the pear-shaped domain.

Eigenvalues	Exact solutions	Approximate solutions
First	0.5000	0.5000
Second	0.1035	0.1050
Third	0.1035	0.1050

TABLE 3
The five reconstructed eigenvalues for the floriform domain.

Eigenvalues	Exact solutions	Approximate solutions
First	0.5000	0.5000
Second	0.3322	0.3300
Third	0.3322	0.3300
Fourth	0.1404	0.1300
fifth	0.1404	0.1300

Then we can locate the local extrema of function (3.23) one by one, starting from the one with the largest magnitude of c_i^+, then the one with the second largest magnitude of c_i^+, and so on. This process provides us with a set of approximate eigenvalues from the knowledge of polarization tensor $M(\lambda, D)$ over γ. We would like to emphasize that only eigenvalues sitting inside the interval $(0.07, 0.53)$ can be reconstructed in our numerical experiment with the choice of γ, considering the fact that γ only encloses such eigenvalues. The exact eigenvalues and the approximate ones obtained by Method 2 described in section 3.1 with $\sigma_0 = 0.05$ are listed in Table 1 for the kite-shaped domain D of the form

$$x = \cos\theta + 0.65\cos 2\theta - 0.65\,, \quad y = 1.5\sin\theta\,, \quad \theta \in (0, 2\pi]\,, \tag{3.23}$$

a pear-shaped domain in Table 2, and a floriform domain with three petals in Table 3. The latter two domains are of the form (3.20) with the same parameter $m = 3$ but a different δ, i.e., $\delta = 0.3$ and 0.6.

As we can observe from Tables 1, 2, and 3, the reconstructed eigenvalues are rather satisfactory and accurate in view of the severe ill-posedness of recovering eigenvalues.

To have a better understanding of the performance of Method 2, we have tried to push our algorithm to the limit and consider a numerically very challenging example with a complicated domain consisting of 12 eigenvalues in the range $(0.07, 0.53)$; see Figure 3 for the shape of this domain. Now, due to the fact that the eigenvalues sit very close to each other, we have chosen a smaller value of $\sigma_0 = 0.02$ to increase the resolution of obtaining eigenvalues from locating local extrema of (3.23). Table 4 shows a comparison between the exact eigenvalues and the approximate ones obtained by our method. Although this example is very challenging, the eigenvalues are still reconstructed with a quite reasonable degree of accuracy, ensuring the reliability of our method in solving this severely ill-posed inverse problem.

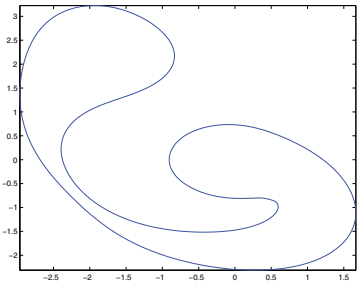

FIG. 3. *Shape of the complicated domain.*

TABLE 4
The 12 *reconstructed eigenvalues for the chosen complicated domain.*

Eigenvalues	Exact solutions	Approximate solutions
First	0.5000	0.5000
Second	0.4820	0.4800
Third	0.4056	0.4050
Fourth	0.3320	0.3150
Fifth	0.2817	0.2850
Sixth	0.2271	0.2050
Seventh	0.1889	0.1850
Eighth	0.1546	0.1400
Ninth	0.1284	0.1250
Tenth	0.1056	0.1050
Eleventh	0.0906	0.0850
Twelfth	0.0762	0.0750

4. Hadamard's formula for Fredholm eigenvalues. In this section, we turn our attention to the optimal shape design problem given the Fredholm eigenvalues corresponding to a geometric shape. Our strategy to approach the problem is via an appropriately formulated Tikhonov regularization. For this purpose, we first discuss how to obtain the shape derivatives of the Neumann–Poincaré operator and the Fredholm eigenvalues. These derivatives are needed when we compute the gradients of the concerned least-squares functional.

To start with, we first derive the shape derivative of the Neumann–Poincaré operator corresponding to a shape D sitting inside a general space $\mathbb{R}^d$ for any $d \geq 1$. The special two-dimensional case was treated in [12]. For the sake of exposition, we shall first introduce some notation. Given a shape D sitting inside $\mathbb{R}^d$, we consider a regular parametrization of the surface ∂D as

$$\begin{aligned} \mathbb{X} : U \subset \mathbb{R}^{d-1} &\to \partial D \subset \mathbb{R}^d, \\ u = (u_1, u_2, ..., u_{d-1}) &\mapsto \mathbb{X}(u)\,. \end{aligned}$$

For notation's sake, we shall often write the vector $\mathbb{X}_i := \frac{\partial \mathbb{X}}{\partial u_i}$. For a given $d-1$ vectors $\{v_i\}_{i=1}^{d-1}$, we shall denote the $d-1$ cross product $\times_{i=1}^{d-1} v_i = v_1 \times v_2 \ldots \times v_{d-1}$ as the dual vector of the functional $\det(\cdot, v_1, v_2, \ldots, v_{d-1})$, i.e., $\langle w, \times_{i=1}^{d-1} v_i \rangle = \det(w, v_1, v_2, \ldots, v_{d-1})$ for any w, which is guaranteed to exist by the Reisz representation theorem. Then, from the fact that $\mathbb{X}$ is regular, we know $\times_{i=1}^{d-1} \mathbb{X}_i$ is nonzero, and the normal vector $\nu := \times_{i=1}^{d-1} \mathbb{X}_i / |\times_{i=1}^{d-1} \mathbb{X}_i|$ is well-defined.

Now consider an ε-perturbation of D, namely, ∂D_ε is given by

$$\partial D_\varepsilon := \{\widetilde{x} \,|\, \widetilde{x} = x + \varepsilon h(u)\nu(x)\,,\ x \in \partial D\}\,, \tag{4.1}$$

with $h \in \mathcal{C}^1(\partial D)$. Let $\Psi_\varepsilon(x) := x + \varepsilon h(u)\nu(x)$ be the diffeomorphism from ∂D to ∂D_ε; then it is easy to see that

$$\begin{aligned} \mathbb{X}^\varepsilon : U \subset \mathbb{R}^{d-1} &\to \partial D_\varepsilon \subset \mathbb{R}^d, \\ u = (u_1, u_2, \ldots, u_{d-1}) &\mapsto \Psi_\varepsilon[u] = \mathbb{X}(u) + \varepsilon h(u)\nu(\mathbb{X}(u)) \end{aligned}$$

is a regular parametrization over ∂D_ε for small ε. Furthermore, directly from the definition, we have $\mathbb{X}_i^\varepsilon = \mathbb{X}_i + \varepsilon \frac{\partial h}{\partial u_i}\nu + \varepsilon h \sum_{j=1}^{d-1} A_{ij}\mathbb{X}_j^\varepsilon$, where the matrix A_{ij} is defined as

$$A := (A_{ij}) = \langle \mathbf{II}(\mathbb{X}_i, \mathbb{X}_j), \nu\rangle\,,$$

and $\mathbf{II}$ is the second fundamental form given by

$$\begin{aligned} \mathbf{II} : T(\partial D) \times T(\partial D) &\to T^\perp(\partial D), \\ \mathbf{II}(v, w) &= -\langle \nabla_v \nu, w\rangle \nu = \langle \nu, \nabla_v w\rangle \nu, \end{aligned}$$

where ∇ is the standard covariant derivative on the ambient space $\mathbb{R}^d$. From the multilinearity and alternating property of the $d-1$ cross product, we can readily calculate at any point $b \in U$ that

$$\times_{i=1}^{d-1}\mathbb{X}_i^\varepsilon(b) = \times_{i=1}^{d-1}\mathbb{X}_i(b) + \varepsilon L(b)[h]\,\big|\times_{i=1}^{d-1}\mathbb{X}_i(b)\big|\,, \tag{4.2}$$

where the vector $L(b)[h]$ is defined as

$$L(b)[h] := \begin{pmatrix} \tilde{\mathbb{X}_1} & \tilde{\mathbb{X}_2} & \cdots & \tilde{\mathbb{X}}_{d-1} & \nu \\ hA_{11} & hA_{12} & \cdots & hA_{1\,d-1} & \varepsilon\frac{\partial h}{\partial u_1} \\ hA_{21} & hA_{22} & \cdots & hA_{2\,d-1} & \varepsilon\frac{\partial h}{\partial u_2} \\ \vdots & \vdots & \ldots & \ddots & \vdots \\ hA_{d-1\,1} & hA_{d-1\,1} & \ldots & hA_{d-1\,d-1} & \varepsilon\frac{\partial h}{\partial u_{d-1}} \end{pmatrix} = \begin{pmatrix} \tilde{\mathbb{X}} & \nu \\ hA & \nabla h \end{pmatrix}$$

and $\tilde{\mathbb{X}}_i := \mathbb{X}_1 \times \mathbb{X}_2 \ldots \times \widehat{\mathbb{X}_i} \ldots \times \mathbb{X}_{d-1} \times \nu$ with the hat meaning the removal of the corresponding vector from the cross product. Hence it yields that

$$\begin{aligned} \langle\,\cdot\,, \nu^\varepsilon(b)\rangle\, d\sigma^\varepsilon(b) &= \langle\,\cdot\,, \times_{i=1}^{d-1}\mathbb{X}_i^\varepsilon(b)\rangle\, db \\ &= \langle\,\cdot\,, \times_{i=1}^{d-1}\mathbb{X}_i(b) + \varepsilon L(b)[h]\,\big|\times_{i=1}^{d-1}\mathbb{X}_i(b)\big|\rangle\, db \\ &= \langle\,\cdot\,, \nu(b) + \varepsilon L(b)[h]\rangle\, d\sigma^\varepsilon(b), \end{aligned} \tag{4.3}$$

where $\nu^\varepsilon(b)$ denotes the normal vector at $\mathbb{X}^\varepsilon(b)$. Moreover, for two arbitrary points $x, y \in \partial D$ given by $x = \mathbb{X}(a), y = \mathbb{X}(b)$ for some $a, b \in U$, we have

$$\mathbb{X}^\varepsilon(a) - \mathbb{X}^\varepsilon(b) = \mathbb{X}(a) - \mathbb{X}(b) + \varepsilon K(a, b)[h],$$

where $K(a, b)[h] := h(a)\nu(a) - h(b)\nu(b)$. Hence, by the Taylor expansion of $|\mathbb{X}^\varepsilon(a) - \mathbb{X}^\varepsilon(b)|^{-d}$ in ε,

$$\begin{aligned} &|\mathbb{X}^\varepsilon(a) - \mathbb{X}^\varepsilon(b)|^{-d} \\ &= \left(|\mathbb{X}(a) - \mathbb{X}(b)|^2 + 2\varepsilon\langle \mathbb{X}(a) - \mathbb{X}(b), K(a, b)[h]\rangle + \varepsilon^2 |K(a, b)[h]|^2\right)^{-d/2} \\ &= |\mathbb{X}(a) - \mathbb{X}(b)|^{-d} - d\,\varepsilon|\mathbb{X}(a) - \mathbb{X}(b)|^{-d-2}\langle \mathbb{X}(a) - \mathbb{X}(b), K(a, b)[h]\rangle + O(\varepsilon^2)\,. \end{aligned} \tag{4.4}$$

Combining (4.3) and (4.4), we obtain the series expression

$$\frac{\langle \mathbb{X}^\varepsilon(a) - \mathbb{X}^\varepsilon(b)\,, \nu^\varepsilon(b)\rangle}{|\mathbb{X}^\varepsilon(a) - \mathbb{X}^\varepsilon(b)|^d}\, d\sigma^\varepsilon(b) := \sum_{n=0}^{\infty} \varepsilon^n \mathbb{K}_{h,n}(a,b)\, d\sigma(b),$$

where

$$\begin{aligned}
\mathbb{K}_{h,0}(a,b) &:= \frac{\langle \mathbb{X}(a) - \mathbb{X}(b)\,, \nu(b)\rangle}{|\mathbb{X}(a) - \mathbb{X}(b)|^d} \\
\mathbb{K}_{h,1}(a,b) &:= \frac{\langle \mathbb{X}(a) - \mathbb{X}(b)\,, L(b)[h]\rangle + \langle K(a,b)[h], \nu(b)\rangle}{|\mathbb{X}(a) - \mathbb{X}(b)|^d} \\
&\quad - d\,\frac{\langle \mathbb{X}(a) - \mathbb{X}(b)\,, K(a,b)[h]\rangle \langle \mathbb{X}(a) - \mathbb{X}(b), \nu(b)\rangle}{|\mathbb{X}(a) - \mathbb{X}(b)|^{d+2}}\,,
\end{aligned}$$

and the higher order terms $\mathbb{K}_{h,i}$ can be explicitly calculated from (4.4) in a similar fashion. Therefore we can see that the kernel of the Neumann–Poincaré operator varies analytically with respect to small ε along any direction $h \in \mathcal{C}^1(\partial D)$.

From now on, whenever the context is clear, by an abuse of notation we will not distinguish between $F(x)$ and $F(a)$ for any function F over ∂D if $x = \mathbb{X}(a) \in \partial D$. Now we define a sequence of integral operators $\mathcal{K}_{D,h}^{(n)}\colon L^2(\partial D) \to L^2(\partial D)$ by

$$\mathcal{K}_{D,h}^{(n)}\phi(x) := \int_{\partial D} \mathbb{K}_{h,n}(x,y)\phi(y) d\sigma(y) \quad \forall\, \phi \in L^2(\partial D) \tag{4.5}$$

for $n \geq 0$. Then we can directly obtain the following result from (4.5).

THEOREM 4.1. *For $N \in \mathbb{N}$, there exists constant C depending only on N, $||\mathbb{X}||_{\mathcal{C}^2}$, and $||h||_{\mathcal{C}^1}$ such that the following estimate holds for any $\widetilde{\phi} \in L^2(\partial D_\varepsilon)$ and $\phi := \widetilde{\phi} \circ \Psi_\varepsilon$:*

$$\left|\left| \mathcal{K}_{\partial D_\varepsilon}^*[\widetilde{\phi}] \circ \Psi_\varepsilon - \mathcal{K}_{\partial D}^*[\phi] - \sum_{n=1}^{N} \varepsilon^n \mathcal{K}_{D,h}^{(n)}[\phi] \right|\right|_{L^2(\partial D)} \leq C\varepsilon^{N+1} ||\phi||_{L^2(\partial D)}\,. \tag{4.6}$$

In particular, the kernel of $\mathcal{K}_{D,h}^{(1)}$ can be explicitly expressed by

$$\begin{aligned}
\mathbb{K}_{h,1}(x,y) &= \frac{\langle x - y\,, L(y)[h]\rangle + \langle K(x,y)[h], \nu(y)\rangle}{|x-y|^d} \\
&\quad - d\,\frac{\langle x - y\,, K(x,y)[h]\rangle \langle x - y, \nu(y)\rangle}{|x-y|^{d+2}}\,,
\end{aligned} \tag{4.7}$$

where $K(x,y)[h] := h(x)\nu(x) - h(y)\nu(y)$ and $\langle v, L(y)[h]\rangle$ can be given explicitly by

$$\langle v, L(y)[h]\rangle = \begin{pmatrix} \alpha & \beta \\ hA & \nabla h \end{pmatrix}$$

for all $v = \sum_{i=1}^{d-1} \alpha_i \mathbb{X}_i + \beta\nu \in \mathbb{R}^d$.

We know now from (4.6) that the shape derivative of the Neumann–Poincaré operator at the variation h and D is given by

$$[\mathcal{D}(\mathcal{K}_{\partial D}^*)](h) = \mathcal{K}_{D,h}^{(1)}\,. \tag{4.8}$$

We would like to remark that the special case of the above theorem for $d = 2$ was treated in [12]. In this special case, the above formulae for $\mathbb{K}_{h,n}$ can be stated

explicitly. With a shape D sitting inside $\mathbb{R}^2$, a parametrization of its boundary can be simplified to be an arc-length parametrization of ∂D, $X(t) : [a, b] \to \partial D$, where $a, b \in \mathbb{R}$ with $a < b$. Let $T(x)$ and $\nu(x)$ be respectively the tangent vector and the outward unit normal to ∂D at $x \in \partial D$, and let $\tau(x)$ be the curvature defined by

$$X''(t) = \tau(x)\nu(x)\,. \tag{4.9}$$

Now for two arbitrary points $x, y \in \partial D$ such that $x = X(t), y = X(s)$ for some $t, s \in [a, b]$, we define

(4.10)
$$F_h(x,y) = \frac{\langle x-y, h(t)x(x) - h(s)\nu(y)\rangle}{|x-y|^2} \quad \text{and} \quad G_h(x,y) = \frac{|h(t)x(x) - h(s)\nu(y)|^2}{|x-y|^2}$$

and define $F_{h,n}$ as the coefficients in the following series:

(4.11)
$$\sum_{n=0}^{\infty} \varepsilon^n F_{h,n}(x,y) := \frac{1}{1 + 2\varepsilon F_h(x,y) + \varepsilon^2 G_h(x,y)} \frac{\sqrt{(1-\varepsilon\tau(y)h(s))^2 + \varepsilon^2 (h'(s))^2}}{\sqrt{(1-\varepsilon\tau(x)h(t))^2 + \varepsilon^2 (h'(t))^2}}\,,$$

where the series converges absolutely and uniformly [12]. We can directly see that

$$F_{h,0}(x,y) = 0 \quad \text{and} \quad F_{h,1}(x,y) = -2F(x,y) + \tau(x)h(x) - \tau(y)h(y)\,. \tag{4.12}$$

Then, following the argument in [12] and using (4.5) and (4.10)–(4.11) we have

$$\begin{aligned}
&\mathbb{K}_{h,0} = \frac{\langle x-y, \nu(x)\rangle}{|x-y|^2}, \quad \mathbb{K}_{h,1} = K_{h,0}F_{h,1} + K_{h,1},\\
&\mathbb{K}_{h,n} = F_{h,n}K_{h,0} + F_{h,n-1}K_{h,1} + F_{h,n-2}K_{h,2}
\end{aligned}$$

for $n \geq 2$, where $K_{h,0}$, $K_{h,1}$, and $K_{h,2}$ are given by

$$\begin{aligned}
K_{h,0} &= \frac{\langle x-y, \nu(x)\rangle}{|x-y|^2},\\
K_{h,1} &= \frac{\langle h(t)\nu(x) - h(s)\nu(y), \nu(x)\rangle}{|x-y|^2} - \frac{\langle x-y, \tau(x)h(t)\nu(x) + h'(t)T(x)\rangle}{|x-y|^2},\\
K_{h,2} &= \frac{\langle h(t)\nu(x) - h(s)\nu(y), \tau(x)h(t)\nu(x) - h'(t)T(x)\rangle}{|x-y|^2}.
\end{aligned}$$

We end this section with the shape derivatives of the Fredholm eigenvalues. Let $\phi_i^{\pm}(D)$ be the orthonormal eigenfunctions of the operator $\mathcal{K}^*_{\partial D}$ with respect to the eigenvalues $\lambda_i^{\pm}(D)$; then we have from the Osborn's theorem [31] that

(4.13)
$$|\lambda_i^{\pm}(D) - \lambda_i^{\pm}(D_\varepsilon) - \langle(\mathcal{K}^*_{\partial D} - \mathcal{K}^*_{\partial D_\varepsilon} \circ \Psi_\varepsilon)\phi_i^{\pm}(D), \phi_i^{\pm}(D)\rangle| \leq C||\mathcal{K}^*_{\partial D} - \mathcal{K}^*_{\partial D_\varepsilon} \circ \Psi_\varepsilon||^2$$

by using the facts that $\mathcal{K}^*_{\partial D_\varepsilon}$ is collectively compact, i.e., $\{\mathcal{K}^*_{\partial D_\varepsilon}[\phi] : ||\phi||_{\mathcal{H}} \leq 1, \varepsilon \geq 0\}$ is sequentially compact, and that $\mathcal{K}^*_{\partial D_\varepsilon}$ converges to $\mathcal{K}^*_{\partial D}$ pointwisely. Now we can easily see from (4.6) and (4.13) the following estimates for the variation of eigenvalues:

$$|\lambda_i^{\pm}(D) - \lambda_i^{\pm}(D_\varepsilon) - \varepsilon\langle\mathcal{K}^{(1)}_{D,h}\phi_i^{\pm}, \phi_i^{\pm}\rangle| \leq C\,\varepsilon^2. \tag{4.14}$$

This yields the following result.

PROPOSITION 4.2. *Let $\lambda_i^{\pm}$ be simple Fredholm eigenvalues; then their shape derivatives are given by*

$$[\mathcal{D}(\lambda_i^{\pm})]\big|_D(h) = \langle \mathcal{K}_{D,h}^{(1)}\phi_i^{\pm}, \phi_i^{\pm}\rangle\,. \tag{4.15}$$

It is worth mentioning that if λ_i is a multiple eigenvalue, it may evolve, under some perturbation, into several separated and distinct eigenvalues. The splitting of eigenvalues may only become apparent at high orders in their Taylor expansions with respect to the perturbation parameter. The splitting in the evaluation of perturbations in λ_i can be studied by arguments similar to the ones in [11, section 3.4].

5. Optimal shape design using partial spectral data.

5.1. Shape design via an appropriate Tikhonov regularization. In this subsection, we formulate our design problem via an optimization framework. We first recall our shape design problem: given a set of eigenvalues $\{\pm\lambda_i(B)\}_{i=1}^N$ corresponding to a target shape B, we intend to find a shape D such that the eigenvalues of the Neumann–Poincaré operator $\mathcal{K}_{\partial D}^*$, denoted as $\lambda_i(D)$, are approximately equal to $\lambda_i(B)$, i.e., $\lambda_i(D) \approx \lambda_i(B)$ for $1 \le i \le N$. In order to achieve this, we have to introduce an appropriate objective functional. In view of the invariance of eigenvalues under rigid transformations and scaling, some effective penalty and regularization terms should be incorporated in the functional to ensure the local existence and uniqueness of the minimizers. This leads us to the following nonlinear functional for our shape design:

$$\begin{aligned}\mathcal{J}_{I,\alpha,\beta}(D) &= \frac{1}{2}\sum_{i=1}^{I} w_i^2|\lambda_i(D)-\lambda_i(B)|^2 + \frac{\alpha}{2}(|D|-1)^2 + \frac{\beta}{2}\left(\int_D 2|x_1|^2 + |x_2|^2\right)\\ &:= (\mathcal{J}_I)_0(D) + \frac{\alpha}{2}\mathcal{A}(D) + \frac{\beta}{2}\mathcal{B}(D)\,,\end{aligned} \tag{5.1}$$

where $I \le N$ is a given integer index, and $\alpha, \beta \in \mathbb{R}^+$ are the parameters for the penalty and the regularization, respectively. In view of the large variation of the magnitudes of eigenvalues, we have also introduced some weights w_i in (5.1), which we will naturally choose to be $w_i = 1/\lambda_i(B)$.

For most existing optimization algorithms, we need to compute the variational derivatives of the functionals involved. For this purpose, we introduce some auxiliary tools.

LEMMA 5.1. *For a given shape D and $f \in L^1(D)$, the shape derivative of the integral*

$$I(D) := \int_D f dx \tag{5.2}$$

is given by

$$[\mathcal{D}I]|_D(h) = \int_{\partial D} fh dt \tag{5.3}$$

at the variation $h \in \mathcal{C}^1(\partial D)$.

Proof. Given a shape D and $a, b \in \mathbb{R}$ with $a < b$, let $X(t) : [a, b] \to \partial D$ be an arc-length parametrization of ∂D and $\nu(x)$ be the outward unit normal to ∂D at $x \in \partial D$.

For a $h \in \mathcal{C}^1(\partial D)$ which is nonzero everywhere, we consider the ε-perturbation D_ε of D as in (4.1). For sufficiently small $\varepsilon > 0$, we consider a change of variables $(x_1, x_2) \mapsto (\tilde{\varepsilon}, t)$ in an ε-tabular neighborhood of ∂D. Denoting $\det(u, v) = \det \left(\begin{smallmatrix} u_1 & v_1 \\ u_2 & v_2 \end{smallmatrix}\right)$ for any $u, v \in \mathbb{R}^2$, then we can write

$$\int_{D_\varepsilon} f dx = \int_0^\varepsilon \int_{\partial D} f \det(X' + \tilde{\varepsilon} h\nu', h\nu) dt d\tilde{\varepsilon} + \int_D f dx \,. \tag{5.4}$$

Using the fact that $X' \perp \nu$ and $\nu' \perp \nu$, we can evaluate the shape derivative of I at h by

$$\begin{aligned} [\mathcal{D}I]|_D(h) &= \frac{\partial}{\partial \varepsilon} \int_{D_\varepsilon} f dx \bigg|_{\varepsilon=0} \\ &= \int_{\partial D} f \det(X' + \varepsilon h\nu', h\nu) dt|_{\varepsilon=0} \\ &= \int_{\partial D} f \det(X', h\nu) dt \\ &= \int_{\partial D} f h dt \,. \end{aligned}$$

This leads to the desired formula. ∎

Using (5.3), we readily know the shape derivative of the following integrals at h:

$$[\mathcal{D}(|D|)](h) = \int_{\partial D} h dt \,, \quad \left[\mathcal{D}\left(\int_D 2|x_1|^2 + |x_2|^2 dx\right)\right](h) = \int_{\partial D} (2|x_1|^2 + |x_2|^2) h dt \,. \tag{5.5}$$

With the above preparations we can now discuss the minimization of functional (5.1). In this work we will focus on the Gauss–Newton method for this minimization. We first introduce some more notions.

Given a shape D and $I \in \mathbb{N}$, we write the vector $\lambda_w(D) = (w_1\lambda_1(D), \ldots, w_I\lambda_I(D))^T$ with the superscript T denoting the transpose and define the Jacobian of the map $D \mapsto \lambda_w(D)$:

$$\begin{aligned} &\mathcal{J}_I|_D : L^2(\partial D) \mapsto \mathbb{R}^I \\ &\qquad \mathcal{J}_I|_D(h) = (w_1[\mathcal{D}\lambda_1]\big|_D(h), \ldots, w_I[\mathcal{D}\lambda_I]\big|_D(h))^T, \end{aligned} \tag{5.6}$$

where $[\mathcal{D}\lambda_i]\big|_D(h)$ is the shape derivative of the Fredholm eigenvalue $\lambda_i(D)$ at h, which can be computed by (4.15). Let $\mathcal{J}_I\big|_D^*$ and $[\mathcal{D}(|D|)]\big|_D^*$ be the respective $L^2(\partial D)$ adjoint of $\mathcal{J}_I\big|_D$ and $[\mathcal{D}(|D|)]\big|_D$; then the Gauss–Newton direction of (5.1) for a shape D can be written as

$$\begin{aligned} N_{I,\alpha,\beta}(D) := &([\mathcal{J}_I\big|_D]^*[\mathcal{J}_I\big|_D])^{-1}\mathcal{J}_I\big|_D^*[\lambda_w(D) - \lambda_w(B)] \\ &+ \alpha[\mathcal{D}(|D|)]\big|_D^*(|D| - 1) + \beta\left[\mathcal{D}\left(\int_D 2|x_1|^2 + |x_2|^2\right)\right]\bigg|_D^* . \end{aligned} \tag{5.7}$$

Now we are ready to formulate the Gauss–Newton method for the minimization of functional (5.1): Let D_n be the nth approximation of the shape D, and let X_n be its arc-length parametrization; then we update X_n by the following iteration:

$$X_{n+1} = X_n - \gamma_n N_{I,\alpha_n,\beta_n}(D_n) \,, \tag{5.8}$$

where γ_n, α_n, and β_n are parameters chosen at each iteration and $N_{I,\alpha_n,\beta_n}(D_n)$ is the Gauss–Newton direction as defined in (5.7) with $\alpha = \alpha_n$ and $\beta = \beta_n$. The choice of parameters γ_n, α_n, and β_n will be discussed in detail in the next subsection.

5.2. Successive refinement for optimization and parameter selection. In this subsection, we describe several detailed strategies for the minimization of the functional $\mathcal{J}_{I,\alpha,\beta}$ in (5.1). These strategies are crucial for our algorithm to work efficiently and to overcome the difficulties arising from the strong nonlinearity and severe ill-posedness of the current shape design problem.

Our first strategy is a successive refinement technique for the minimization. This strategy is motivated by our observations from numerical experiments. Due to the strong nonlinearity and ill-posedness, iteration (5.8) may stop at some local minima of (5.1) when $I \in \mathbb{N}$ is large. On the other hand, for small I, we observe that iteration (5.8) converges often to a global minimum of (5.1) rapidly even with a poor initial guess. But functional (5.1) does not capture fine features of the target shape if I is too small. These observations motivate us with the following successive refinement strategy: We first minimize $\mathcal{J}_{I,\alpha,\beta}$ in (5.1) with $I = 2$, then minimize $\mathcal{J}_{I,\alpha,\beta}$ for $I = 3, \ldots, N$ recursively by using the minimizer of $\mathcal{J}_{I-1,\alpha,\beta}$ as an initial guess. As we will see in our numerical experiments, this strategy works very effectively in avoiding the trapping of the minimization process at some local minima as well as providing us with more fine details for our shape design.

The next strategy is on the choice of parameters α_n and β_n for iteration (5.8). α_n and β_n should be chosen such that the contributions on the search directions in (5.8) from three parts $(\mathcal{J}_I)_0(D)$, $\mathcal{A}(D)$, and $\mathcal{B}(D)$ in (5.1) are balanced at each iteration. Under these considerations, a possible choice is that we first fix two small positive constants C_1 and C_2, then update α_n and β_n at each iteration by

$$\alpha_n = C_1 \frac{(\mathcal{J}_I)_0(D_n)}{\mathcal{A}(D_n)}, \quad \beta_n = C_2 \frac{(\mathcal{J}_I)_0(D_n)}{\mathcal{B}(D_n)}. \tag{5.9}$$

Our last strategy is on the choice of step size γ_n along the Gauss–Newton direction $N_{I,\alpha_n,\beta_n}(D_n)$, for which we will carry out the line search, namely,

$$\gamma_n = \operatorname{argmin}\left\{\mathcal{J}_{I,\alpha_n,\beta_n}(X_n - \gamma N_{I,\alpha_n,\beta_n}(D_n)) : \gamma \in \mathbb{R}^+\right\}. \tag{5.10}$$

Combining the above three strategies, we arrive at the successive refinement Gauss–Newton shape design algorithm.

Reconstruction algorithm.

Step 1. Given a tolerance ε and an initial guess $D_{1,0}$.

Step 2. For $I = 1$ to N,

Step 2.1. Set $n := 1$;

Step 2.2. Compute $\alpha_{I,n}$, $\beta_{I,n}$ as in (5.9);

Step 2.3. Compute the Gauss–Newton direction $N_{I,\alpha_n,\beta_n}(D_{I,n})$ as in (5.7); Find the step size γ_n as in (5.10); Then update $X_{I,n}$ by

$$X_{I,n+1} = X_{I,n} - \gamma_{I,n} N_{I,\alpha_n,\beta_n}(D_{I,n});$$

Step 2.4. If $|\mathcal{J}_{I,\alpha_n,\beta_n}(X_{I,n}) - \mathcal{J}_{I,\alpha_n,\beta_n}(X_{I,n+1})| < \varepsilon$, set $D_{I,\text{stab}} := D_{I,n+1}$; otherwise set $n := n + 1$ and go to Step 2.2;

Step 2.5. Take $D_{I+1,0} := D_{I,\text{stab}}$.

Step 3. Find $n_0 \in \{1, 2, .., N\}$ such that $D_{n_0,\text{stab}}$ has the minimal residue:

$$(\mathcal{J}_N)_0(D_{n_0,\text{stab}}) = \min_{I\in\{1,2,..,N\}} \left\{(\mathcal{J}_N)_0(D_{I,\text{stab}})\right\}.$$

Output $D_{n_0,\text{stab}}$ and stop.

5.3. Numerical experiments. In this section, we shall present several numerical examples to check the performance of the newly proposed reconstruction algorithm in section 5.2 for the optimal shape design using partial spectral data.

Given a domain D, we first obtain the observed data of the forward problem, the Fredholm eigenvalues of D, as in section 3.2. In order to test the robustness of our reconstruction algorithm, we introduce some multiplicative random noise in the eigenvalues of the forward problem as follows:

$$\lambda_i^\sigma = \lambda_i(1 + \sigma\,\xi)\,, \quad i = 1, \ldots, N\,, \tag{5.11}$$

where ξ is uniformly distributed between –1 and 1 and σ corresponds to the level of the noise in the data, which is always set to be 1% in all our examples. For each of the examples, we conduct the same experiment with 50 independent realizations of multiplicative noise. Then we apply our reconstruction algorithm for shape reconstruction with the noisy data. As the eigenvalues are invariant under scaling, rotation, and translation, a postprocessing of scaling, rotating, and translating is performed for better comparisons between the reconstructed and exact shapes. The relative error of each independent realization is then defined by

$$\text{Relative Error} := \frac{\text{Area}\,((D^{\text{reconstruct}} \bigcup D)\backslash(D^{\text{reconstruct}} \bigcap D))}{\text{Area}(D)} \tag{5.12}$$

and the shape of each realization can then be classified by its relative error based on the standard derivation of the statistical data obtained. Because of the strong ill-posedness, the perturbations in the eigenvalues often lead to great changes in numerical reconstructions. However, it is quite interesting to us that for each example we demonstrate in this section, we obtain only two basic shapes by our reconstruction algorithm, and all the other shapes obtained with a different set of random noise are basically of very small perturbations, quantified by (5.12), around these two basic shapes. It may indicate the robustness and effectiveness of our chosen regularization formulation. Because of these observations, we shall present only the two basic shapes for each example, each of which *represents* a class of its perturbed shapes achieved in our reconstructions. Clear statistics showing this classification of all reconstructed shapes into these two basic shapes together with the average relative error and its standard deviation of each class are tabulated. In our choices of α_n, β_n, and tolerance ε, we take $C_1 = C_2 = 0.01$ in (5.9), and $\varepsilon = 5 \times 10^{-4}$. And we will take the first seven eigenvalues in the observed data, namely, $N = 7$ in our reconstructions.

Example 1. This example tests an ellipse of the form (3.19) as the target shape; see Figure 4(a). Table 5 tabulates the relative errors of the reconstructed shapes after 50 independent realizations of random noise, classified into two classes. Figures 4(c) and 4(d) show the two basic shapes achieved by our reconstructions. The initial guess in the reconstruction is a shape of the form (3.20) with $\delta = 0.6$, $m = 5$, $K_2 = 1$; see Figure 4(b). Clearly this is a very poor initial shape, but the reconstructed shapes seem quite satisfactory.

TABLE 5
Statistical result of reconstructed shapes in Example 1.

Results	Frequency	Mean relative error	Standard deviation of relative error
Figure 4(c)	54%	11.59%	0.0113
Figure 4(d)	46%	5.37%	0.0103
Total	100 %	8.73%	0.0332

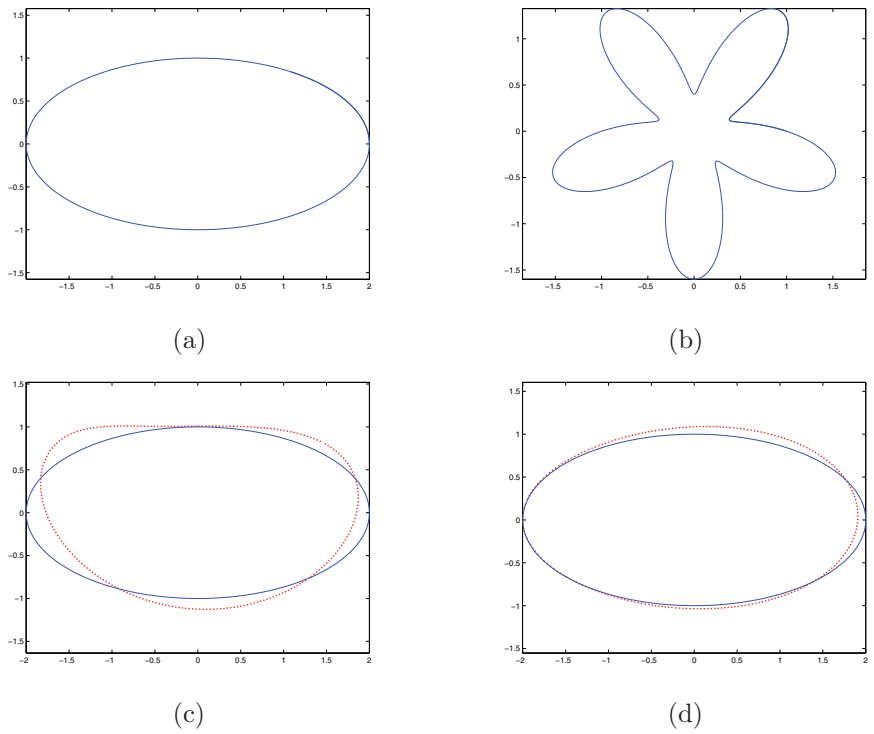

FIG. 4. (a) *Target shape in Example* 1*;* (b) *initial guess;* (c), (d) *two basic shapes in reconstructions after* 50 *independent realizations of* 1% *random noise (exact shape in blue, reconstructed shape in red).*

Example 2. In this example, our target shape is a heart-shaped domain of the form (3.20) with $\delta = 0.8$, $m = 1$, $K_2 = 1$; see Figure 5(a). Table 6 shows the relative errors of the reconstructed shapes after 50 independent realizations of random noise, classified into two classes. Starting with a very poor initial guess, a shape of the form (3.20) with $\delta = 0.6$, $m = 7$, $K_2 = 1$ (see Figure 5(b)), the two basic shapes achieved in our reconstructions with different sets of random noise are shown in Figures 5(c) and 5(d). Considering the invariance of the target shape up to translation, rotation, and scaling, our reconstructions seem to be very satisfactory, and our algorithm is able to reconstruct the correct dimensions and the shape of the target rather accurately.

Example 3. A peanut-shaped domain of the form (3.20) with $\delta = 0.6$, $m = 2$, $K_2 = 1$ is investigated in this example; see Figure 6(a). Our initial guess is of the form (3.20) with $\delta = 0.6$, $m = 5$, $K_2 = 1$; see Figure 6(b). Figure 6(c) and Figure 6(d) present the two basic shapes achieved in our reconstructions with different sets of random noise. The relative errors of the reconstructed shapes are tabulated in Table 7. This example is actually rather numerically challenging, considering the

TABLE 6
Statistical result of reconstructed shapes in Example 2.

Results	Frequency	Mean relative error	Standard deviation of relative error
Figure 5(c)	52%	5.15%	0.0104
Figure 5(d)	48%	5.43 %	0.0112
Total	100 %	5.28%	0.0109

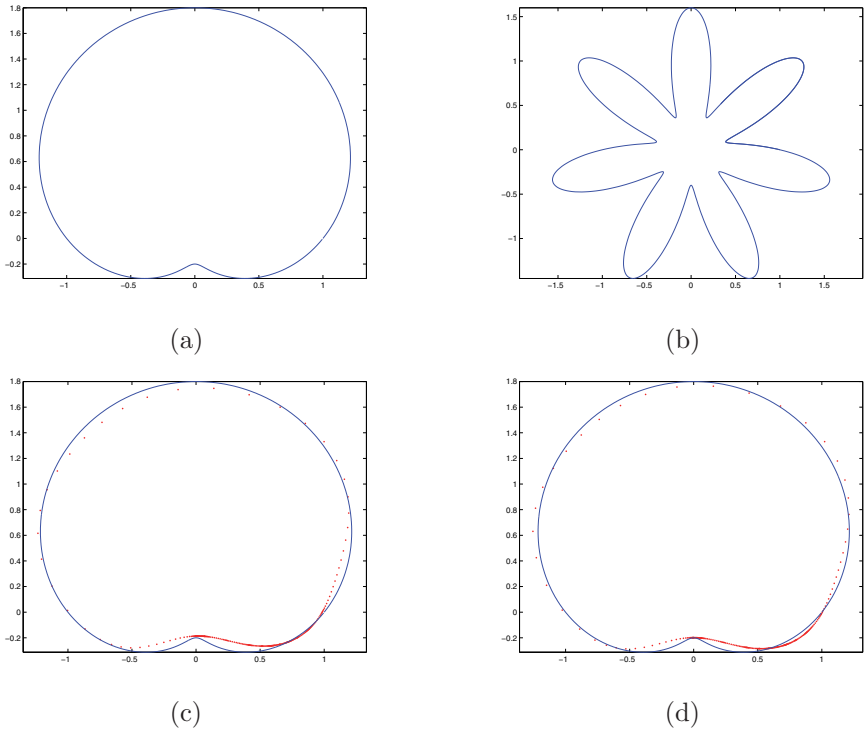

FIG. 5. (a) *Target shape in Example* 2; (b) *initial guess;* (c), (d) *two basic shapes in reconstructions after* 50 *independent realizations of* 1% *random noise (exact shape in blue, reconstructed shape in red).*

TABLE 7
Statistical result of reconstructed shapes in Example 3.

Results	Frequency	Mean relative error	Standard deviation of relative error
Figure 6(c)	54%	24.78%	0.0115
Figure 6(d)	46%	28.11 %	0.0124
Total	100 %	26.31%	0.0121

fact that the peanut shape has two small and sharp concave dips. Notwithstanding the high sensitivity and ill-posedness of the eigenvalue shape reconstruction problem and the very challenging nature of target shape, the reconstructed results still seem to be rather satisfactory, providing necessary and recognizable features of the peanut.

Example 4. In this example, we consider a pear-shaped domain of the form (3.20) with $\delta = 0.3$, $m = 3$, $K_2 = 1$; see Figure 7(a). We start from the initial guess of the form (3.20) with $\delta = 0.6$, $m = 3$, $K_2 = 1$; see Figure 7(b). The two basic shapes

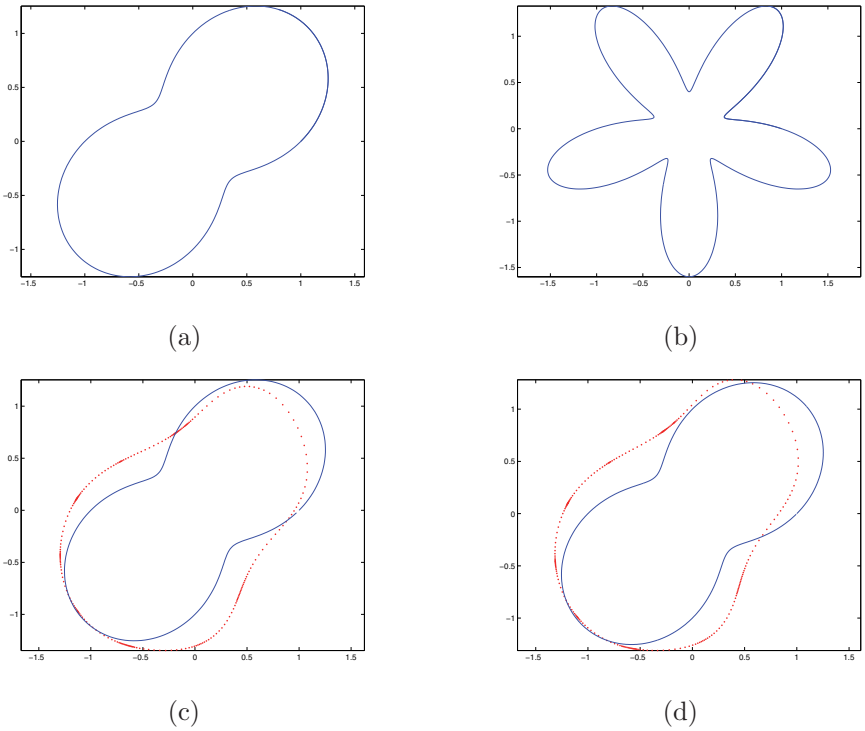

FIG. 6. (a) *Target shape in Example* 3*;* (b) *initial guess;* (c), (d) *two basic shapes in reconstructions after* 50 *independent realizations of* 1% *random noise (exact shape in blue, reconstructed shape in red).*

TABLE 8
Statistical result of reconstructed shapes in Example 4.

Results	Frequency	Mean relative error	Standard deviation of relative error
Figure 7(c)	52%	3.20%	0.0097
Figure 7(d)	48%	3.32 %	0.00103
Total	100 %	3.26%	0.0099

achieved in our reconstructions from the data polluted by different sets of random noise are shown in Figure 7(c) and Figure 7(d). Table 8 presents the relative errors of the reconstructed shapes. Considering the random noise added in the spectral data and the sensitivity of eigenvalue problem, our reconstructions prove to be quite satisfactory.

6. Concluding remarks. In this work we have proposed numerical methods to recover the Fredholm eigenvalues of a domain from the measurements of its polarization tensor at multiple contrasts or frequencies. Then we have developed an optimal shape design algorithm (up to rigid transformations and scaling) based on partial knowledge of Fredholm eigenvalues. Both inverse problems are highly nonlinear and severely ill-posed, but our numerical experiments have demonstrated the effectiveness and robustness of the proposed reconstruction algorithms. By using only the first few Fredholm eigenvalues, we have regularized the considered inverse problems. We expect that our results will have important applications in plasmon resonant

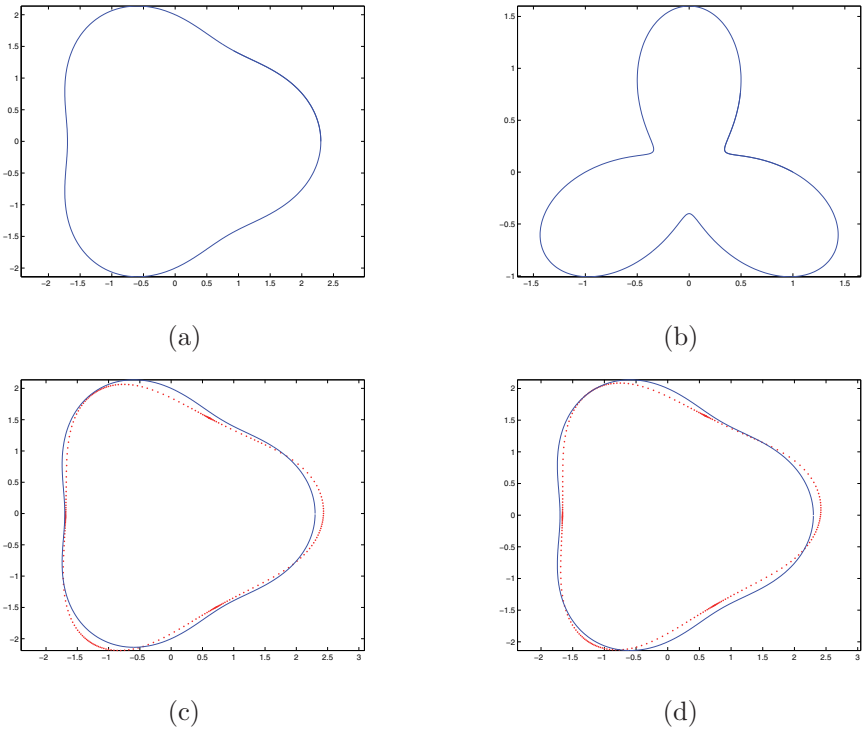

FIG. 7. (a) *Target shape in Example* 4; (b) *initial guess;* (c), (d) *two basic shapes in reconstructions after* 50 *independent realizations of* 1% *random noise (exact shape in blue, reconstructed shape in red).*

nanoparticle design and in multifrequency imaging and classification of small anomalies from electrical capacitance measurements.

Appendix A. Pulsed imaging. In this section, we show how to acquire the polarization tensor at multiple contrasts in electrical capacitance tomography using pulsed imaging. To begin with, we first introduce the governing equation of the voltage potential in the electrosensing electrical capacitance tomography problem [13], which reads, for any given final time $T > 0$,

$$\text{(A.1)} \qquad \begin{cases} \nabla \cdot \left(\sigma + \varepsilon\, \partial_t\right) \nabla u(x,t) = f(x,t) & \text{in } (0,T) \times \mathbb{R}^2, \\ u(x,t) = O(|x|^{-1}) & \text{as } |x| \to \infty \, \forall t \in (0,T), \\ u(0,x) = u_\iota(x) & \text{in } \mathbb{R}^d\,. \end{cases}$$

In what follows we assume D is an open bounded domain in $\mathbb{R}^2$ of class $\mathcal{C}^{1,\alpha}$ $(0 < \alpha < 1)$, and the conductivity and permittivity coefficients σ and ε are piecewise constant respectively of the form

$$\sigma = \sigma_c \chi(D) + \sigma_m \chi(\mathbb{R}^2 \backslash \overline{D}) \quad \text{and} \quad \varepsilon = \varepsilon_c \chi(D) + \varepsilon_m \chi(\mathbb{R}^2 \backslash \overline{D})\,,$$

where σ_c and ε_c are respectively the conductivity and permittivity of D, whereas $\sigma_m > 0$, $\varepsilon_m \geq 0$ are the background values. The solution to (A.1) is shown in [13] to be unique in the Banach space $H^1\left((0,T), H^1_{\text{loc}}(\mathbb{R}^2)\right)$ if $u_\iota \in H^1(\mathbb{R}^2)$ and

$f \in H^1\left((0,T), H^{-1}(\mathbb{R}^2)\right)$. Our aim is to reconstruct the polarization tensor from the measurements of the solutions $u(x,t)$ to (A.1).

For the sake of brevity, we consider the initial condition $u_\iota = 0$ and the source current f of the physically interesting form

$$f(t,x) = h(t)\tilde{f}(x) := h(t)\left(\sum_{j=1}^{p} a_j \delta_0(x - x_s^j)\right),$$

where δ_0 is the Dirac mass located at 0, and $h \in \mathcal{S}(\mathbb{R})$ is a casual function sitting inside the classical Schwartz space, compactly supported in $(0,T)$, and represents the time profile of the source. Function $\tilde{f}$ models an electric organ, say, of a fish, with source points $x_s^j \in \mathbb{R}^2 \backslash \overline{D}$ and intensities a_j at x_s^j satisfying the neutrality condition $\sum_{j=1}^{p} a_j = 0$.

Suppose that $u_0(x,t)$ is the solution to (A.1) with the homogeneous medium $\sigma = \sigma_m$ and $\varepsilon = \varepsilon_m$. Then following the argument in [13], we can apply the Fourier transform to (A.1) in the temporal domain, together with the single layer potential formalism as introduced in section 2, to yield the following identity of the scattered field in the frequency domain:

$$\hat{u}(\omega,x) - \hat{u_0}(\omega,x) = \hat{h}(\omega) \sum_{n,m=1}^{\infty} A_{sm} \hat{M}_{mn}(\omega, D) B_n^T(x), \tag{A.2}$$

where ω is the operating frequency, and $\{A_{sm}\}$ and $\{B_n(x)\}$ are the vectors of the form

$$A_{sm} = \sum_{j=1}^{p} \frac{a_j}{2\pi m |x_s^j|} \left(\cos(m\theta_{x_s^j}),\ \sin(m\theta_{x_s^j})\right),$$

$$B_n(x) = \frac{1}{2\pi n |x|} \left(\cos(n\theta_x),\quad \sin(n\theta_x)\right) \tag{A.3}$$

and the matrices

$$\hat{M}_{mn}(\omega, D) = \begin{pmatrix} \hat{M}_{mn}^{cc}(\omega, D) & \hat{M}_{mn}^{cs}(\omega, D) \\ \hat{M}_{mn}^{sc}(\omega, D) & \hat{M}_{mn}^{ss}(\omega, D) \end{pmatrix}$$

are the Fourier transforms in the space of tempered distributions $\mathcal{S}'(\mathbb{R})$ of the time-dependent generalized polarization tensor defined by [13]:

$$\hat{M}_{mn}^{cs}(\omega) = \int_{\partial D} S_n(y) \left(\lambda(\omega) I - \mathcal{K}_D^*\right)^{-1} \left[\frac{\partial}{\partial \nu} C_m\right](y) d\sigma(y), \tag{A.4}$$

where $\lambda(\omega)$ is the admittivity given by

$$\lambda(\omega) := \frac{1}{2}\left(\frac{(\sigma_c + \sigma_m) + i(\varepsilon_c + \varepsilon_m)\omega}{(\sigma_c - \sigma_m) + i(\varepsilon_c - \varepsilon_m)\omega}\right), \tag{A.5}$$

and C_m and S_m denote the real and imaginary parts of the harmonic polynomial $(x_1 + ix_2)^m$, respectively. The other components $\hat{M}_{mn}^{cc}$, $\hat{M}_{mn}^{sc}$, and $\hat{M}_{mn}^{ss}$ in $\hat{M}_{mn}(\omega, D)$ are defined in a similar manner.

Next we will derive the polarization tensor at multiple contrasts from pulsed imaging. We notice directly from the previously defined polarization tensor $M(\lambda(\omega),$

$D) = (M_{ij}(\lambda(\omega), D))_{i=1,2}$ (see (2.16)), that it coincides with the Fourier transform of the first order time-dependent generalized polarization tensor $\hat{M}_{11}(\omega, D)$, namely,

$$\begin{pmatrix} M_{11}(\lambda(\omega), D) & M_{12}(\lambda(\omega), D) \\ M_{21}(\lambda(\omega), D) & M_{22}(\lambda(\omega), D) \end{pmatrix} = \begin{pmatrix} \hat{M}_{11}^{cc}(\omega, D) & \hat{M}_{11}^{cs}(\omega, D) \\ \hat{M}_{11}^{sc}(\omega, D) & \hat{M}_{11}^{ss}(\omega, D) \end{pmatrix}. \tag{A.6}$$

Now, consider the scattered fields $u^c(x, \theta_s, t)$ from the measurement events with receivers on a circle of radius R_x, 2 two source points with polar coordinates (R_s, θ_s), $(R_s, \pi - \theta_s)$, and intensities $a_1 = -a_2 = \frac{1}{2}$; then following (A.2), (A.4), and (A.6), we can derive

$$M_{12}(\lambda(\omega)) = \frac{R_s R_x}{\hat{h}(\omega)} \mathfrak{F}_{\theta_s}^c \circ \mathfrak{F}_{\theta_x}^s \circ \mathfrak{F}_t(u^c - u_0)[1, 1, \omega],$$

where $\mathfrak{F}_t$ is the temporal Fourier transform with kernel $\exp(i\omega t)$, whereas $\mathfrak{F}_\theta^c$ and $\mathfrak{F}_\theta^s$ are respectively the spatial Fourier transform with kernels $\cos(m\theta)$ and $\sin(m\theta)$. With the help of the scattered fields $u^s(x, \theta_s, t)$ from another set of measurement events with two source points $(R_s, \pm\theta_s)$ and intensities $a_1 = -a_2 = \frac{1}{2}$, the other three entries of $M(\lambda(\omega), D)$ can also be obtained similarly. The general representation of polarization tensor at multiple contrasts then reads as follows:

$$M_{ij}(\lambda(\omega)) = \frac{R_s R_x}{\hat{h}(\omega)} \mathfrak{F}_{\theta_s}^{\eta_i} \circ \mathfrak{F}_{\theta_x}^{\eta_j} \circ \mathfrak{F}_t(u^{\eta_i} - u_0)[1, 1, \omega], \tag{A.7}$$

where $\eta_i = c$ for $i = 1$ and $\eta_i = s$ for $i = 2$. This simple formula is used to recover the polarization tensor at contrasts $\lambda(\omega)$ from pulsed imaging.

Now, consider the curve $\gamma := \{\lambda(\omega) \in \mathbb{C} : \omega \in \mathbb{R}\}$ given by (A.5); then this smooth simple closed curve gives rise to a circle with diameter passing through the points $\frac{1}{2}\frac{\sigma_m + \sigma_c}{\sigma_m - \sigma_c}$ and $\frac{1}{2}\frac{\varepsilon_m + \varepsilon_c}{\varepsilon_m - \varepsilon_x}$ on the complex plane. Therefore γ encloses the spectrum of $\sigma(\mathcal{K}_{\partial D}^*) \subset (-1/2, 1/2]$ whenever $\sigma_m - \sigma_c$ and $\varepsilon_m - \varepsilon_c$ have different signs. Clearly, this enables us to recover the eigenvalues of $\sigma(\mathcal{K}_{\partial D}^*)$ from $M(\lambda, D)$ as discussed in subsection 3.1.

The results above can be naturally extended to three dimensions.

Appendix B. Multiply connected objects. In this section, we briefly investigate the eigenvalue of the Neumann–Poincaré operator of a domain consisting of two identical copies of a nonoverlapping shape with $\mathcal{C}^{1,\alpha}$ boundary and the same contrast. Consider a given shape D_1, and define the shape

$$D_v := D_1 \bigcup D_2, \tag{B.1}$$

where $D_2 := D_1 + v$, with $v \in \mathbb{R}^2$ being a vector such that the distance $d(D_1, D_2)$ between D_1 and D_2 is positive. The Neumann–Poincaré operator $\mathbb{K}_{\partial D_v}^*$ associated with D_v is given by [6]

$$\mathbb{K}_{\partial D_v}^* := \begin{pmatrix} \mathcal{K}_{\partial D_1}^* & \frac{\partial}{\partial \nu_1} \mathcal{S}_{\partial D_2} \\ \frac{\partial}{\partial \nu_2} \mathcal{S}_{\partial D_1} & \mathcal{K}_{\partial D_2}^* \end{pmatrix}. \tag{B.2}$$

As we will observe numerically later in this section, the number of connected components and the multiplicity of eigenvalue $\frac{1}{2}$ are the same, which is briefly described below.

For the sake of exposition, we first define the space $\mathcal{H} = (L^2(\partial D_v), \langle \mathcal{S}_{\partial D_v} \cdot, \cdot \rangle)$ and $\mathcal{H}_0 = \mathcal{H} \bigcap \{\int_{\partial D_v} \phi \, d\sigma = 0\}$, then $\mathcal{H} = \mathcal{H}_0 \oplus \mathbb{R}^2$. The Neumann–Poincaré operator $\mathbb{K}^*_{\partial D_v}$ is then self-adjoint in $\mathcal{H}$ considering the fact that a generalized version of Calderon identity holds [6]. We also consider the double layer potential operator

$$\mathcal{D}_{\partial D}[\phi](x) = \int_{\partial D} \frac{\partial}{\partial \nu} \Gamma(x-y)\phi(y)\, d\sigma(y)\,, \quad x \in \mathbb{R}^d \backslash \partial D\,, \tag{B.3}$$

which has the following well-known jump condition:

$$\mathcal{D}^{\pm}_{\partial D}[\phi](x) = \left(\mp \frac{1}{2} + \mathcal{K}_{\partial D} \right)[\phi](x)\,, \quad x \in \partial D\,. \tag{B.4}$$

Then, by an integration by parts, we directly obtain that the L^2-adjoint of the operator $\mathbb{K}^*_{\partial D_v}$ is given by

$$\mathbb{K}_{\partial D_v} = \begin{pmatrix} \mathcal{K}_{\partial D_1} & \mathcal{D}_{\partial D_2} \\ \mathcal{D}_{\partial D_1} & \mathcal{K}_{\partial D_2} \end{pmatrix}. \tag{B.5}$$

Now following the arguments in [5], we consider the equation $\left(\lambda I - \mathbb{K}^*_{\partial D_v}\right)\chi = 0$ with $\chi = (\chi_1, \chi_2) \in \mathcal{H}$. We integrate the two equations in this linear system on ∂D_i for $i = 1, 2$ respectively and use (B.5) together with $\mathcal{D}_{\partial D_i}[1] = 0$ on ∂D_j and $\mathcal{K}_{\partial D_i}[1] = \frac{1}{2}$ on ∂D_i to obtain $\left(\lambda - \frac{1}{2}\right)\left(\int_{\partial D_1} \chi_1 d\sigma, \int_{\partial D_2} \chi_2 d\sigma\right) = 0$. This implies either $\lambda = \frac{1}{2}$ or ($\lambda \neq \frac{1}{2}$ and $\chi \in \mathcal{H}_0$); hence we know that $\frac{1}{2}I - \mathbb{K}^*_{D_v}$ is invertible in $\mathcal{H}_0$.

With the above knowledge, we can explicitly construct the eigenfunctions corresponding to the eigenvalue $\frac{1}{2}$, thereby show the multiplicity of the eigenvalue is indeed 2 following the arguments in [6]. Indeed, since $\frac{1}{2}I - \mathbb{K}^*_{\partial D_v}$ is invertible in $\mathcal{H}_0$, there exist the unique solutions $\psi_i := (\psi_i^1, \psi_i^2) \in \mathcal{H}_0$ to the equation

$$\left(\frac{1}{2}I - \mathbb{K}^*_{D_v}\right)\psi_i = \frac{\partial \mathcal{S}^-_{D_i}[1]}{\partial \nu} \in \mathcal{H}_0, \tag{B.6}$$

where we have also used the fact that $\int_{\partial D_i} \frac{\partial \mathcal{S}^-_{D_i}[1]}{\partial \nu^j} d\sigma = 0$ for $j = 1, 2$. Consider now $\phi_i := \psi_i + \delta_i$ for $\delta_i := (\delta_{i1}, \delta_{i2})$ with δ_{ij} being the Kronecker delta. Then from the fact that $-\frac{\partial \mathcal{S}^-_{D_i}[1]}{\partial \nu} = \left(\frac{1}{2}I - \mathbb{K}^*_{D_v}\right)\delta_i$, we can see $\left(\frac{1}{2}I - \mathbb{K}^*_{D_v}\right)\phi_i = 0$. This proves that ϕ_i are the corresponding eigenfunctions for the eigenvalue $\frac{1}{2}$. Now by a direct integration, we have $\int_{\partial D_i} \phi_j d\sigma = |\partial D_j| \delta_{ij}$, and $\{\phi_i\}_{i=1,2}$ are hence linear independent. Since $\mathcal{H}_0$ has co-dimension 2 and $\frac{1}{2}I - \mathbb{K}^*_{D_v}$ is invertible in $\mathcal{H}_0$, the multiplicity of $\frac{1}{2}$ is 2.

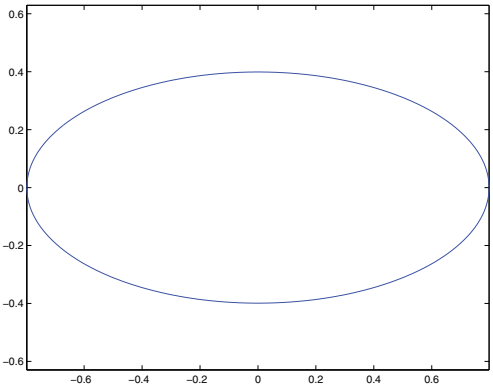

FIG. 8. *The ellipse* D_1 .

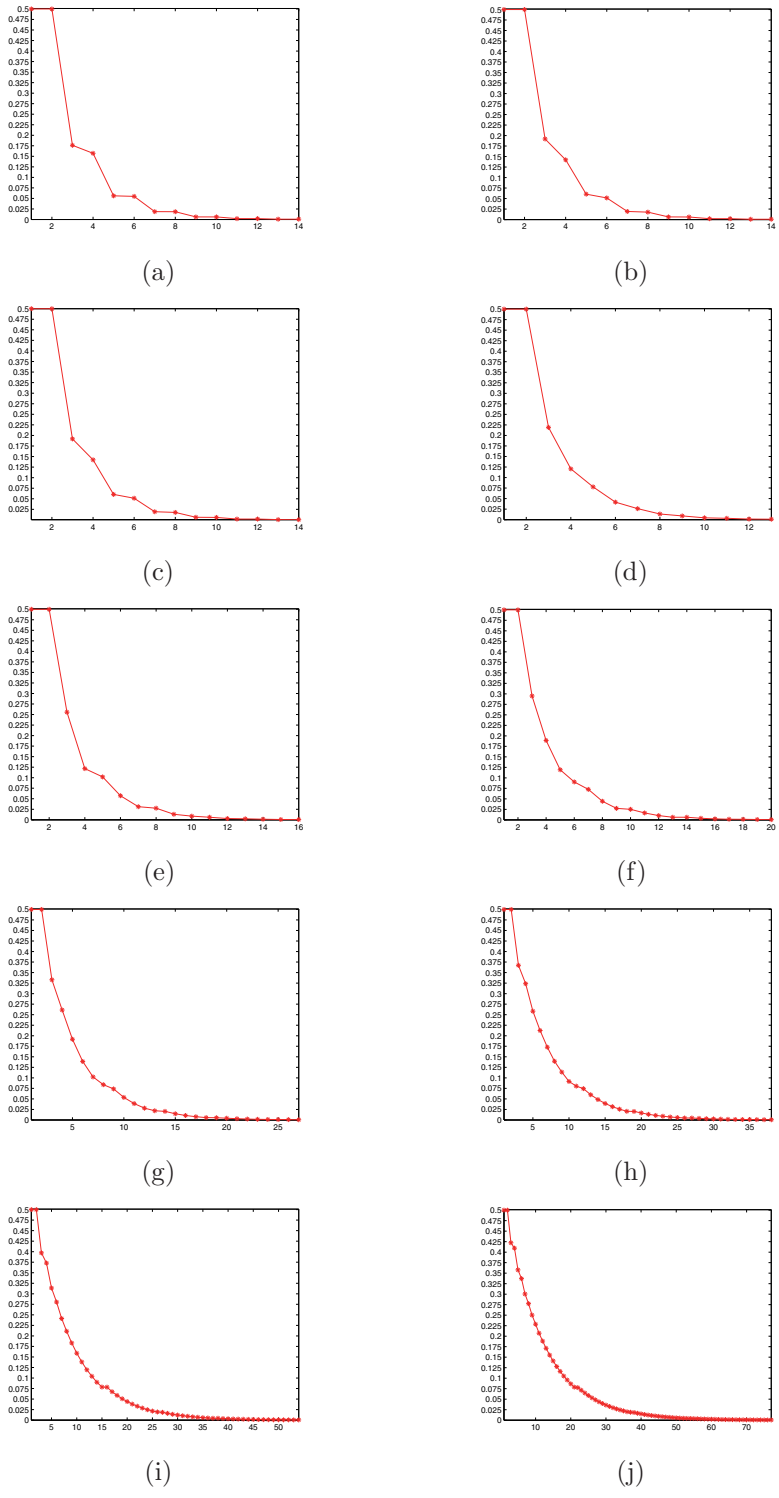

FIG. 9. *Spectrum of* $\mathbb{K}^*_{\partial D_v}$ *in* (B.2) *as* $k = 5 - n$ *with* $n = 1, 2, \ldots, 10$, *starting from* (a) *with* $n = 1$ *to* (j) *with* $n = 10$.

We remark that one can use the same technique to show the multiplicity of the eigenvalue $\frac{1}{2}$ of a Neumann–Poincaré operator $\mathbb{K}^*_{\partial D}$ of a domain D with N connected component is N, therefore establishing the relationship between the number of connected components and the multiplicity of eigenvalue $\frac{1}{2}$; we refer to [5, 6, 15] for more details.

In addition to the aforementioned property of the Fredholm eigenvalues, we are also interested in how the eigenvalues of $\mathbb{K}^*_{\partial D_v}$ behave as v varies, and particularly when $d(D_1, D_2) \to 0$. As an example, we consider an ellipse, D_1, of the form (3.19) (see Figure 8).

Letting $v = (2^k + 2)(0, 1)$, where $k = 5 - n$ and $n = 1, 2, \ldots, 10$, we observe the change of the spectrum of $\mathbb{K}^*_{\partial D_v}$. As v varies, Figure 9 shows those eigenvalues of $\mathbb{K}^*_{\partial D_v}$ which are larger than 0.0005.

We can observe numerically that the spectrum gradually forms a smoother curve, and the multiplicity of the eigenvalue $1/2$ reflects the number of connected components of D_v as demonstrated earlier.

Acknowledgment. The authors would like to thank two anonymous referees for their many insightful and constructive comments and suggestions, which have led to a great improvement of the results and organization of this work.

REFERENCES

[1] L. V. Ahlfors, *Remarks on the Neumann-Poincaré integral equation*, Pacific J. Math., 3 (1952), pp. 271–280.

[2] H. Ammari, T. Boulier, and J. Garnier, *Modeling active electrolocation in weakly electric fish*, SIAM J. Imaging Sci., 5 (2013), pp. 285–321.

[3] H. Ammari, T. Boulier, J. Garnier, W. Jing, H. Kang, and H. Wang, *Target identification using dictionary matching of generalized polarization tensors*, Found. Comput. Math., 14 (2014), pp. 27–62.

[4] H. Ammari, T. Boulier, J. Garnier, and H. Wang, *Shape identification and classification in electrolocation*, Proc. Natl. Acad. Sci. USA, 111 (2014), pp. 11652–11657.

[5] H. Ammari, G. Ciraolo, H. Kang, H. Lee, and G. W. Milton, *Spectral theory of a Neumann-Poincaré-type operator and analysis of cloaking due to anomalous localized resonance*, Arch. Ration. Mech. Anal., 208 (2013), pp. 667–692.

[6] H. Ammari, G. Ciraolo, H. Kang, H. Lee, and K. Yun, *Spectral analysis of the Neumann-Poincaré operator and characterization of the stress concentration in anti-plane elasticity*, Arch. Ration. Mech. Anal., 208 (2013), pp. 275–304.

[7] H. Ammari, Y. Deng, and P. Millien, *Surface plasmon resonance of nanoparticles and applications in imaging*, arXiv:1412.3656, 2014.

[8] H. Ammari, J. Garnier, W. Jing, H. Kang, M. Lim, K. Solna, and H. Wang, *Mathematical and Statistical Methods for Multistatic Imaging*, Lecture Notes in Math. 2098, Springer-Verlag, New York, 2013.

[9] H. Ammari, J. Garnier, H. Kang, M. Lim, and S. Yu, *Generalized polarization tensors for shape description*, Numer. Math., 126 (2014), pp. 199–224.

[10] H. Ammari and H. Kang, *Polarization and Moment Tensors: With Applications to Inverse Problems and Effective Medium Theory*, Appl. Math. Sci. 162, Springer, New York, 2007.

[11] H. Ammari, H. Kang, and H. Lee, *Layer Potential Techniques in Spectral Analysis*, Math. Surveys Monogr. 153, AMS, Providence, RI, 2009.

[12] H. Ammari, H. Kang, M. Lim, and H. Zribi, *The generalized polarization tensors for resolved imaging. Part* I*: Shape reconstruction of a conductivity inclusion*, Math. Comp., 81 (2012), pp. 367–386.

[13] H. Ammari and H. Wang, *Time domain multiscale shape identification in electro-sensing*, arXiv:1409.3714, 2014.

[14] R. D. Benguria, H. Linde, and B. Loewe, *Isoperimetric inequalities for eigenvalues of the Laplacian and the Schrdinger operator*, Bull. Math. Sci., 2 (2012), pp. 1–56.

[15] E. Bonnetier and F. Triki, *Pointwise bounds on the gradient and the spectrum of the Neumann-Poincaré operator: The case of* 2 *discs*, in Multi-Scale and High-Contrast PDE: From Modelling, to Mathematical Analysis, to Inversion, Contemp. Math. 577, AMS, Providence, RI, 2012, pp. 81–91.

[16] E. Bonnetier and F. Triki, *On the spectrum of the Poincaré variational problem for two close-to-touching inclusions in* 2*D*, Arch. Ration. Mech. Anal., 209 (2013), pp. 541–567.

[17] J. Flusser, T. Suk, B. Zitov, and I. Ebrary, *Moments and Moment Invariants in Pattern Recognition*, Wiley Online Library, 2009.

[18] D. Grieser, *The plasmonic eigenvalue problem*, arXiv:1208.3120, 2012.

[19] J. Helsing and K. M. Perfekt, *On the polarizability and capacitance of the cube*, Appl. Comp. Harmonic Anal., 34 (2013), pp. 445–468.

[20] C. D. Hopkins and G. W. M. Westby, *Time domain processing of electrical organ discharge waveforms by pulse-type electric fish*, Brain Behav. Evol., 29 (1986), pp. 77–104.

[21] M. K. Hu, *Visual pattern recognition by moment invariants*, Trans. Inform. Theor., 8 (1962), pp. 179–187.

[22] P. K. Jain, K. S. Lee, I. H. El-Sayed, and M. A. El-Sayed, *Calculated absorption and scattering properties of gold nanoparticles of different size, shape, and composition: Applications in biomedical imaging and biomedicine*, J. Phys. Chem. B, 110 (2006), pp. 7238–7248.

[23] S. X. Liao and M. Pawlak, *On image analysis by moments*, IEEE Trans. Pattern Anal. Mach. Intellig., 18 (1996), pp. 254–266.

[24] H. Kang and J. K. Seo, *Inverse conductivity problem with one measurement: Uniqueness of balls in* $\mathbb{R}^3$, SIAM J. Appl. Math., 59 (1999), pp. 851–867.

[25] O. D. Kellogg, *Foundations of Potential Theory*, Grundlehren Math. Wiss. 31 Springer-Verlag, Berlin, 1967.

[26] D. Khavinson, M. Putinar, and H. S. Shapiro, *Poincaré's variational problem in potential theory*, Arch. Ration. Mech. Anal., 185 (2007), pp. 143–184.

[27] S. Kim, J. Lee, J. K. Seo, E. J. Woo, and H. Zribi, *Multifrequency trans-admittance scanner: Mathematical framework and feasibility*, SIAM J. Appl. Math., 69 (2008), pp. 22–36.

[28] T. Kotnik, D. Miklavcic, and T. Slivnik, *Time course of transmembrane voltage induced by time-varying electric fields: A method for theoretical analysis and its application*, Bioelectrochemistry Bioenergetics, 45 (1998), pp. 3–16.

[29] I. D. Mayergoyz, D. R. Fredkin, and Z. Zhang, *Electrostatic (plasmon) resonances in nanoparticles*, Phys. Rev. B, 72 (2005), 155412.

[30] I. D. Mayergoyz and Z. Zhang, *Numerical analysis of plasmon resonances in nanoparticules*, IEEE Trans. Mag., 42 (2006), pp. 759–762.

[31] J. E. Osborn, *Spectral approximation for compact operators*, Math. Comp., 29 (1975), pp. 712–725.

[32] D. Sarid and W. A. Challener, *Modern Introduction to Surface Plasmons: Theory, Mathematica Modeling, and Applications*, Cambridge University Press, New York, 2010.

[33] M. Schiffer, *The Fredholm eigen values of plane domains*, Pacific J. Math., 7 (1957), pp. 1187–1225.

[34] M. Schiffer and G. Schober, *An extremal problem for the Fredholm eigenvalues*, Arch. Ration. Mech. Anal., 44 (1971/72), pp. 83–92.

[35] J. K. Seo and E. J. Woo, *Multi-frequency electrical impedance tomography and magnetic resonance electrical impedance tomography*, in Mathematical Modeling in Biomedical Imaging I, Lecture Notes in Math. 1983, Springer-Verlag, Berlin, 2009, pp. 1–71.

[36] G. Springer, *Fredholm eigenvalues and quasiconformal mapping*, Acta Math., 111 (1964), pp. 121–142.